



HAL
open science

Response of magnesium microcrystals to c-axis compression and contraction loadings at low and high strain rates

Nicolò Maria Della Ventura, Amit Sharma, Cyril Cayron, Szilvia Kalácska, Thomas E.J. Edwards, Cinzia Peruzzi, Manish Jain, Julia T Pürstl, Roland E Logé, Johann Michler, et al.

► To cite this version:

Nicolò Maria Della Ventura, Amit Sharma, Cyril Cayron, Szilvia Kalácska, Thomas E.J. Edwards, et al.. Response of magnesium microcrystals to c-axis compression and contraction loadings at low and high strain rates. *Acta Materialia*, In press, pp.118762. 10.1016/j.actamat.2023.118762 . emse-03992384

HAL Id: emse-03992384

<https://hal-emse.ccsd.cnrs.fr/emse-03992384v1>

Submitted on 21 Nov 2023

HAL is a multi-disciplinary open access archive for the deposit and dissemination of scientific research documents, whether they are published or not. The documents may come from teaching and research institutions in France or abroad, or from public or private research centers.

L'archive ouverte pluridisciplinaire **HAL**, est destinée au dépôt et à la diffusion de documents scientifiques de niveau recherche, publiés ou non, émanant des établissements d'enseignement et de recherche français ou étrangers, des laboratoires publics ou privés.



Distributed under a Creative Commons Attribution 4.0 International License

Response of magnesium microcrystals to c-axis compression and contraction loadings under low and high strain rate conditions

Nicolò M. della Ventura ^{a,*} (first and corresponding author: nicolo.dellaventura@empa.ch)

Amit Sharma ^a (second author: amit.sharma@empa.ch)

Cyril Cayron ^b (third author: cyril.cayron@epfl.ch)

Szilvia Kalácska ^{a,d} (fourth author: szilvia.kalacska@cnrs.fr)

Thomas E. J. Edwards ^a (fifth author: thomas.edwards@empa.ch)

Cinzia Peruzzi ^a (sixth author: cinzia.peruzzi@empa.ch)

Manish Jain ^a (seventh author: manish.jain@empa.ch)

Julia T. Pürstl ^c (eighth author: jtp35@cam.ac.uk)

Roland E. Logé ^b (ninth author: roland.loge@epfl.ch)

Johann Michler ^a (tenth author: johann.michler@empa.ch)

Xavier Maeder ^a (eleventh author: xavier.maeder@empa.ch)

- a) Empa, Swiss Federal Laboratories for Materials Science and Technology, Laboratory for Mechanics of Materials and Nanostructures, Feuerwerkerstrasse 39, 3602, Thun, Switzerland
- b) Laboratory of ThermoMechanical Metallurgy (LMTM), PX Group Chair, Ecole Polytechnique Fédérale de Lausanne (EPFL), Rue de la Maladière 71b, 2000 Neuchâtel, Switzerland
- c) Department of Materials Science and Metallurgy, University of Cambridge, 27 Charles Babbage Road, Cambridge, CB3 0FS, United Kingdom
- d) Mines Saint-Etienne, Univ Lyon, CNRS, UMR 5307 LGF, Centre SMS, 158 cours Fauriel 42023, Saint-Étienne, France

* Corresponding author: E-mail: nicolo.dellaventura@empa.ch, Tel: +41794545862;

Abstract:

In this work, 99.999% pure magnesium (Mg) single microcrystal structures have been deformed in c-axis compression and contraction conditions at room temperature under loading rates from 5×10^{-4} up to $\sim 590 \text{ s}^{-1}$ and 45 s^{-1} , respectively, allowing to evaluate the strain rate sensitivity and apparent activation volume of prismatic and pyramidal slip systems. In c-axis contraction, under at strain rates of 45 s^{-1} , the formation of a new grain whose crystallographic characteristics do not correspond to those of well-known twin systems, calls for the use of the *weak twinning* theory, introduced by Cayron. Through transformation matrices, a solution that requires the breakdown of the invariant plane strain condition emerged, suggesting that a unit cell reconstruction has taken place via pyramidal II to basal plane transformation. This unconventional twin can be related to a classical simple shear

twin, the $\{10\bar{1}5\}$ twin, by a 2.1° angular correction. In c -axis compression, at the highest applied strain rate, no twin has been detected in $5\mu\text{m}$ sized pillars of 2:1 (height to width) aspect ratio. Plasticity is thus mediated purely by slip. However, the appearance of newly oriented grains is observed by lowering the sample size or by reducing the aspect ratio, whose crystallographic features suggest a recently proposed mechanism of unit cell reconstruction through the transformation from pyramidal I to basal plane. The present manuscript urges for the use of the new crystallographic *weak twinning* theory.

1. Introduction

Deformation twinning in hexagonal-close-packed (hcp) crystal is strongly dependent on the loading direction with respect to the crystallographic c -axis [1,2]. In magnesium (Mg) and its alloys, two types of c -axis twins are commonly reported, $\{10\bar{1}2\}\{10\bar{1}1\}$ tension (TTW) and $\{10\bar{1}1\}\{10\bar{1}2\}$ compression (CTW). The critical resolved shear stress (τ_{CRSS}) of TTW is lower than that for CTW [3]. The occurrence of TTW during c -axis tensile loading is the primary mode for accommodating the plastic deformation, and CTW during c -axis compression is known to be a minor deformation mechanism at room temperature [4–6].

CTWs have been generally observed during compression of extruded or hot-rolled polycrystalline specimens with different textures and grain sizes [3,7–9]. Due to the variation in grain orientation, the presence of grain boundaries, pre-existing twin boundaries and other complexities, externally applied and locally perceived stress states may differ, resulting in a very difficult assessment of the stress tensor at CTW nucleation sites and limiting their understanding. In the past, to overcome this problem, c -axis macro and microscale compression tests were performed on single crystal of pure Mg [4–6]. Indeed, although the τ_{CRSS} for slip on the close-packed basal plane is significantly lower than for the prismatic and pyramidal π_1 and π_2 planes, basal slip can be suppressed during c -axis compression due to a null Schmid factor, which favours the activity of other deformation modes, including CTW. Surprisingly, despite the uniaxial compressive stress field in such tests, CTWs occur occasionally in areas of high stress concentration in the form of thin, needle-like lamellae, while pyramidal slip activity largely governs plasticity [5,10,11]. This has an important effect on the mechanical response of Mg. The large build-up of internal strains accommodated by limited and harder deformation modes leads to lower ductility at high strain levels and thus induces material failure, making c -axis compression the most detrimental loading condition in Mg. Nevertheless, $[0001]$ compression of a single-crystal sample efficiently allows for investigating of strain rate sensitivities (SRSs) of non-basal slip systems and, in principle, of CTWs. To this end, as twinning is suspected to be less strain rate sensitive compared to slip [12–16], and higher stress states can be reached at smaller scales, the easier activation of CTW at higher deformation rates could be suspected and could help to shed a light into the so-called "lack of CTWs".

In Mg high-stress conditions can also favour the nucleation of particular "new grains". Indeed, apart from slip and deformation twinning, another way of accommodating plasticity during c -axis compression of Mg was introduced very recently in the form of *deformation graining* [17]. In particular, Liu et al. [17] observed that the displacements of atoms occurring due to either the high-stress loading conditions, due to the exhaustion of dislocation mediated plasticity at high strain levels or both, induce a "hybrid diffusive-displacive" mode of deformation that results in the nucleation of a newly oriented grains, not corresponding to deformation twins, that enhance plasticity by means of activation of other deformation modes (slip and twinning) within them, improving the machinability of Mg and

reducing crack nucleation. This mechanism cannot be directly related to deformation twinning because the existence of an invariant twin plane is not established [18]. Nevertheless, also alternative origins of this mechanism have been proposed. In view of the numerous evidences of unusual parent-new grain misorientations and inconsistent twin interfaces that have been reported and discussed in the last decade [19,20], Cayron [21] suggested that the concept of deformation twins needs to be extended to martensitic transformations without diffusion - the shuffles are just the movements of the atoms in the lattice that do not obey the same linear law as the nodes of the lattices, and hence not related to diffusion-based mechanisms. Thus, the phenomenon of *deformation graining* can be understood without diffusion as a martensitic mechanism, setting the basis of the recently introduced *weak twinning* concept [22]. In particular, *weak twinning* refers to a mechanism in which the interface is not anymore necessarily fully invariant as for usual deformation twinning, and can be slightly distorted to be transformed into a new non-equivalent plane.

In order to further investigate the afore-mentioned research areas, micropillar compression in [0001] and micro-tensile tests in $[\bar{1}010]$ orientations were performed under loading rates from 5×10^{-4} up to $\sim 590 \text{ s}^{-1}$ and 45 s^{-1} , respectively. The shape and position of testing structures close to the edge of the sample, allowed precise characterizations of the crystallographic orientation by Electron Backscatter Diffraction (EBSD) both before and after testing. The experiments required the redesign of the quasi-static and high strain rate (HSR) testing rigs, making them suitable for both compression and tensile loadings at the microscale, limiting divergences in the compliance of the test machines. The choice of loading directions allows for further study of the direction-dependent micro-mechanical response of Mg by observing the material behaviour during *c*-axis direct and indirect straining (*c*-axis compression and contraction, respectively). In particular, *c*-axis compression refers to when the externally applied stress field has a component along the [0001] direction, whilst *c*-axis contraction when the [0001] axis is reduced by the effect of a strain. This implies that *c*-axis compression and *c*-axis contraction have different associated strain fields, and hence different values of interaction work, W [23]. Russell *et al.* [7] suggested that the onset of CTW may be facilitated under *c*-axis contraction compared to *c*-axis compression due to a lower τ_{CRSS} attributed to differences in the stresses experienced by the unit cell. This behaviour was ascribed by the authors to the greater hydrostatic pressure in the case of contraction compared to the case of uniaxial *c*-axis compression, favouring the complex shuffles required for this twinning mode. As CTWs manifest themselves as thin and needle-like lamellae, as already observed above, 3D EBSD reconstructions have been performed to ensure the eventual "lack of CTW" through the whole thickness of some deformed structures. A thorough investigation of the possible nucleation of new *weak twins* is also presented. Irrespective to the formation of CTW or *weak twins*, the current study nevertheless allows to evaluate the *SRS* and apparent activation volume (V^*) of non-basal slip systems in pure Mg at the microscale in both loading modes.

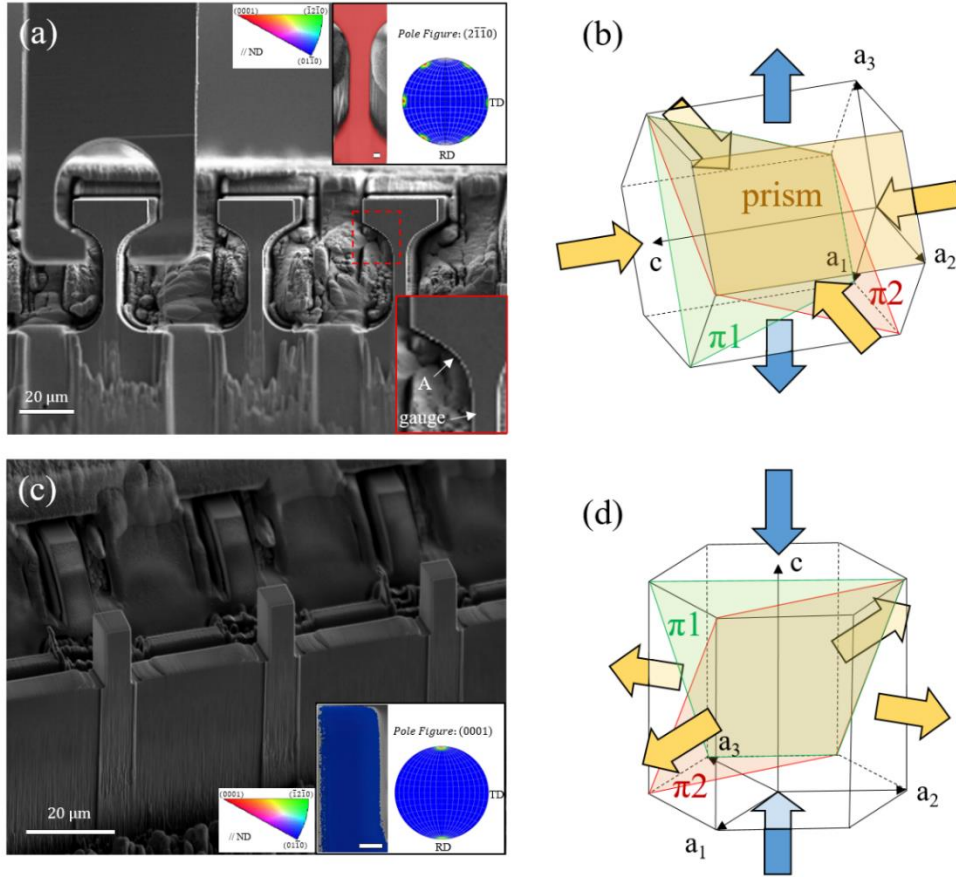


Figure 1: Images of the structures fabricated by focused ion beam (FIB) and the corresponding crystallographic orientations. (a,c) Single crystal microtensile and micropillar samples prepared at the specimen edge allowing EBSD before and after deformation on the front surface of the structures. The EBSD maps and pole figures in the inserts show the respective crystal orientations. (b,d) Stress and strain fields of the crystal during $[\bar{1}010]$ extension (b) and $[0001]$ compression (d). The blue arrows indicate the externally applied stress; the yellow arrows refer to the strains induced by the action of the applied load. The slip planes along which the deformation is expected to take place are highlighted in the crystals. All undefined scale bars correspond to $2\ \mu\text{m}$. The inverse pole figure (IPF) colour code refers to the out-of-plane crystal direction (ND, normal direction).

2. Materials and methods

A 99.999% pure, fully single-crystalline Mg sample (PSC, Easton, USA) was mechanically polished to $1\ \mu\text{m}$ and then electro-polished at 12 V with a refrigerated (10°C) electrolyte, comprised of 85% ethanol, 5% HNO_3 and 10% HCl . The sample was then used for microtensile bar (T-bar or Tb) and micropillar fabrication using a Ga^+ focused ion beam (FIB) microscope (Tescan, Lyra3) with gauge cross-section dimensions of $5 \times 5\ \mu\text{m}^2$ for both structure types, and height of $20\ \mu\text{m}$ and $10\ \mu\text{m}$, respectively (see Figure 1). Two additional sets of pillars have been fabricated with gauge cross-section dimensions of (i) $1.2 \times 1.2\ \mu\text{m}^2$ with 2:1 height to width aspect ratio, and (ii) $5 \times 5\ \mu\text{m}^2$ with 3:2 aspect ratio (tolerance on dimensions: $\pm 100\text{nm}$). To avoid curtaining artifacts on the lateral surfaces of the structures, a 200 nm thick ion-beam deposited platinum layer was applied on top of them. The cross-section area was used to calculate the engineering stresses. Stresses and strains (σ , ε) are nominal. The structures were fabricated at the front surface of the bulk sample, allowing for EBSD acquisitions before and after the deformation. The micromechanical tests were conducted using dedicated *in situ* Alemnis nanoindenter set-ups for quasi-static and HSR conditions [24] mounted inside a scanning electron microscope (SEM, Tescan Lyra3). The tensile tests

were then performed along the $[\bar{1}010]$ axis at different strain rates using a silicon gripper [25], whereas along the $[0001]$ axis in compression with a nanoindenter fitted with a 20 μm diameter doped diamond flat punch. In HSR compression, the testing rig employs a piezo-electric load sensor, where the flat punch was mounted, rather than the standard strain gauges-based load cell used at low strain rates in the conventional testing conditions ($< 1 \text{ s}^{-1}$). In tension, however, the piezo-electric load sensor was mounted on the sample side.

After micromechanical testing, several micropillars were lifted out and thinned down in order to provide an overview of the textural development upon deformation. Transmission Kikuchi Diffraction (TKD) maps were recorded using an EDAX DigiView camera with 2×2 binning ($442 \times 442 \text{ px}^2$). For this, an electron beam of 30 kV and 10 nA was applied. After the TKD map acquisitions, further thinning was performed for atomic resolution imaging using a ThermoFischer Themis 200 G3 aberration (probe) corrected Transmission Electron Microscope (TEM) operating at 200 kV. For some pillars, scanning precession electron diffraction (SPED) has been used to generate high spatial resolution orientation/phase maps with a DigiSTAR system from NanoMEGAS company (Brussels, Belgium) equipped in the same aberration-corrected TEM. A step size of 7 nm was used to reveal the nanoscale characteristics.

Three-dimensional EBSD reconstructions of two deformed tensile structures have been performed to detect and reconstruct the complete shape and spatial distribution of the grains that constitute the entire crystallographic morphology within the specimen. This was done using post-mortem EBSD acquisitions together with FIB tomography in a static setup [26]. In this case, EBSD maps were acquired with a Symmetry detector and the Aztec 4.1 software (Oxford Instrument, UK), with 20kV using 7nA beam conditions and 150 nm step size. EBSD maps were captured after every FIB slice of 200 nm from the front surface throughout the thickness of the structure. FIB slicing was done at 30kV and 1nA. Photoshop CC 2017 was used to manually align the slices by changing the visibility of one slice over the other. Amira v5.2 software was used to create the 3D reconstructions from the 2D maps.

3. Results

Figure 1a,c shows the $(2\bar{1}\bar{1}0)$ and (0001) pole figures for the T-bar and pillar structures. The chosen reference system for the hcp unit cell (**a**₁, **a**₂, **c**) can be seen in Figure 1b,d. The Schmid factor (m_{SF}), τ_{CRSS} and $\sigma_y = \tau_{CRSS}/m_{SF}$ (yield stress) values to predict the possible and preferred modes of deformation are reported in Table 1. In both the cases basal activity is inhibited through $m_{SF_basal} = 0$. The value of τ_{CRSS} for the $\{10\bar{1}2\}$ twin mode reported for bulk Mg in the literature is low ($\sim 12 \text{ MPa}$) [27], however, the unidirectionality of twinning in hcp hinders its formation in c-axis compression. Thus, although the τ_{CRSS} for $\langle a \rangle$ prismatic, $\langle c+a \rangle$ pyramidal 1st and 2nd order slip planes are much higher (Table 1), they remain the only possible modes of accommodating the plastic deformation, together with CTW.

Table 1: m_{SF} and τ_{CRSS} of the slip and twin systems considered for $[\bar{1}010]$ extension and $[0001]$ compression of Mg structures.

Mode	crystal direction	plane	experimental τ_{CRSS} (MPa)	$\langle \bar{1}010 \rangle$ tension		$\langle 0001 \rangle$ compression	
				m_{SF}	σ_y (MPa)	m_{SF}	σ_y (MPa)

Basal	$\langle \bar{1}2\bar{1}0 \rangle$	(0001)	0.52-0.81 [28,29]	0	-	0	-
Prismatic <a>	$\langle \bar{1}2\bar{1}0 \rangle$	(10 $\bar{1}$ 0)	39-50 [30,31]	0.44	88-113	0	-
Pyramidal I <c+a>	$\langle 2\bar{1}\bar{1}3 \rangle$	($\bar{1}$ 011)	40-44 [32,33]	0.41	97-107	0.41	97-107
Pyramidal II <c+a>	$\langle \bar{1}2\bar{1}3 \rangle$	(11 $\bar{2}$ 2)	80 [34]	0.35	225	0.45	177
CTW	$\langle 10\bar{1}2 \rangle$	(10 $\bar{1}$ 1)	115 [3]	0.43	267	0.43	267

3.1 $[\bar{1}010]$ tension (c-axis contraction)

In tension, the deformation behaviour is characterized by a series of discrete load drops in the stress-strain curve and a simultaneous hardening and/or stress plateau (Figure 2a-c). In all tests, the first load drop occurred with the onset of yield after elastic loading and has been therefore used to determine the τ_{CRSS} of the corresponding activated deformation mode. The variation of the τ_{CRSS} with strain rate, from which the *SRS* is derived at yield ($SRS = \frac{\partial \ln(\tau)}{\partial \ln(\dot{\epsilon})}$), is reported in Figure 2d. The calculated values of *SRS* are ~ 0.01 and ~ 0.046 for the range of strain rates investigated here, which correspond to values of apparent activation volume (V^*) (using Eq. (1)) of $2.36 \pm 0.2 \text{ nm}^3$ and $0.43 \pm 0.07 \text{ nm}^3$, respectively. Here,

$$V^* = k_B T \left. \frac{\partial \ln \dot{\epsilon}}{\partial \tau_{CRSS}} \right|_T \quad (1)$$

with k_B the Boltzmann constant and T the temperature at which the test was performed (293 K).

The SEM images reported in Figure 3 show an overview of the processes that assisted plastic deformation of the microtensile structures at the different applied strain rates. For a specific loading condition, different strain values have been applied intentionally in order to avoid the specimen break and allow for post-test observations of the different deformation stages. Slip traces at the front and lateral surfaces of the structures can be attributed to the activation of prismatic planes (Figure 3e, Tb05). It was thus revealed that prismatic slip represents the predominant mode accommodating the plastic deformation during $[\bar{1}010]$ microtensile loadings. Expressing therefore V^* in terms of b^3 , with b the Burgers vector of <a> prismatic dislocation ($b = 0.3209 \text{ nm}$), the apparent activation volume was found to be $\sim 72b^3$ for $\dot{\epsilon} \leq 10^{-1} \text{ s}^{-1}$ and $\sim 13b^3$ above. It should be noted that the experimental determination of V^* is of primary importance as it is related to the area swept by the dislocation and it is indicative of the dislocation mobility mechanism. In particular, as evidenced by the reduction of V^* , the help of the applied stress to overcome the energy barrier for dislocation motion becomes significant at higher strain rate, which is caused by the greater contribution of dislocation inertia (kinetic energy imparted from strain energy and stored in the moving core).

Furthermore, at the highest applied strain rate (45 s^{-1}) and for the most strained structure (Tb09), a new thin and needle-like lamellar grain was formed (Grain 1). EBSD analyses in Figure 3f,g suggest that the matrix (Grain 0) and the new grain are related by a $\sim 44^\circ (\pm 1^\circ)$ misorientation around the a -axis, in short: (44° , a -axis). This does not correspond to the 56.2° expected in the occurrence of CTW. Giving the confined nature of Grain 1, it is important to ascertain whether other new grains, not detectable at the front surface of the specimens, have developed within structures deformed at lower strain rates. Thus, with the intent of performing a more complete and accurate

analysis, a 3D reconstruction has been made for Tb01 as well as for Tb09, which represent the most strained structures at the lowest and highest applied strain rate (Supp. Figure S-1). From these reconstructions, no other grain was observed apart from Grain 1 in Tb09. Moreover, the latter disappears after the first 200 nm below the front surface (after the first FIB slice in the process of the 3D reconstruction – see section 2). An *in situ* video of a tensile test carried out at the highest imposed strain rate can be found in Supplementary Video 1.

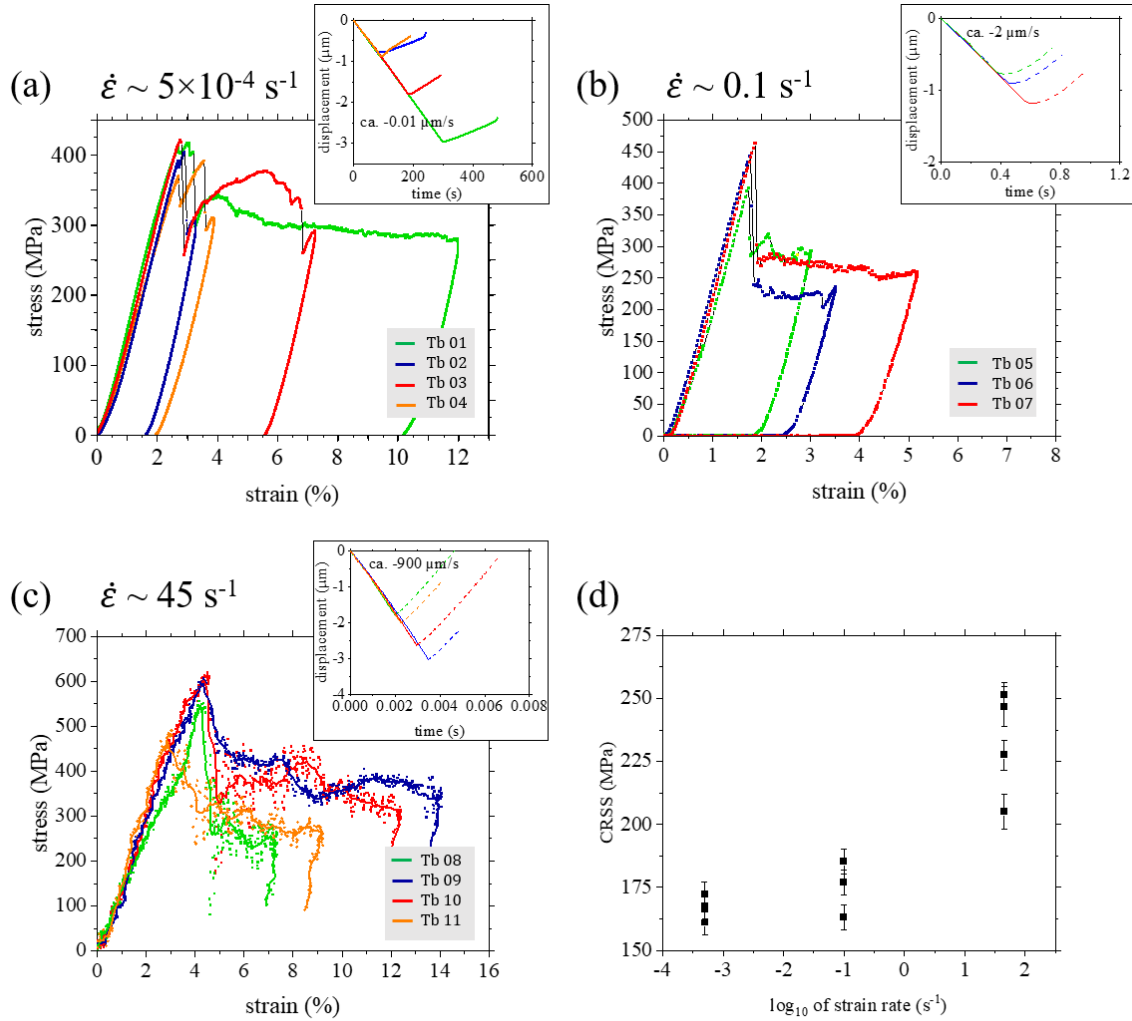


Figure 2: Stress-strain curves related to $[\bar{1}010]$ tensile tests at different strain rates (5×10^{-4} to 45 s^{-1}) (a-c). The inserts illustrate the displacement vs time curves from which the strain rate has been calculated considering a characteristic height of $20 \mu\text{m}$. For further information regarding the displacement calibration procedure, refer to [25]. The variation of the τ_{CRSS} with strain rate is shown in (d). The value of τ_{CRSS} has been measured in correspondence of the stress that preceded the load drop detected in (a-c). Note that the error bars consider also uncertainties ($\pm 100 \text{ nm}$) in the SEM measures of the dimensions of the structures.

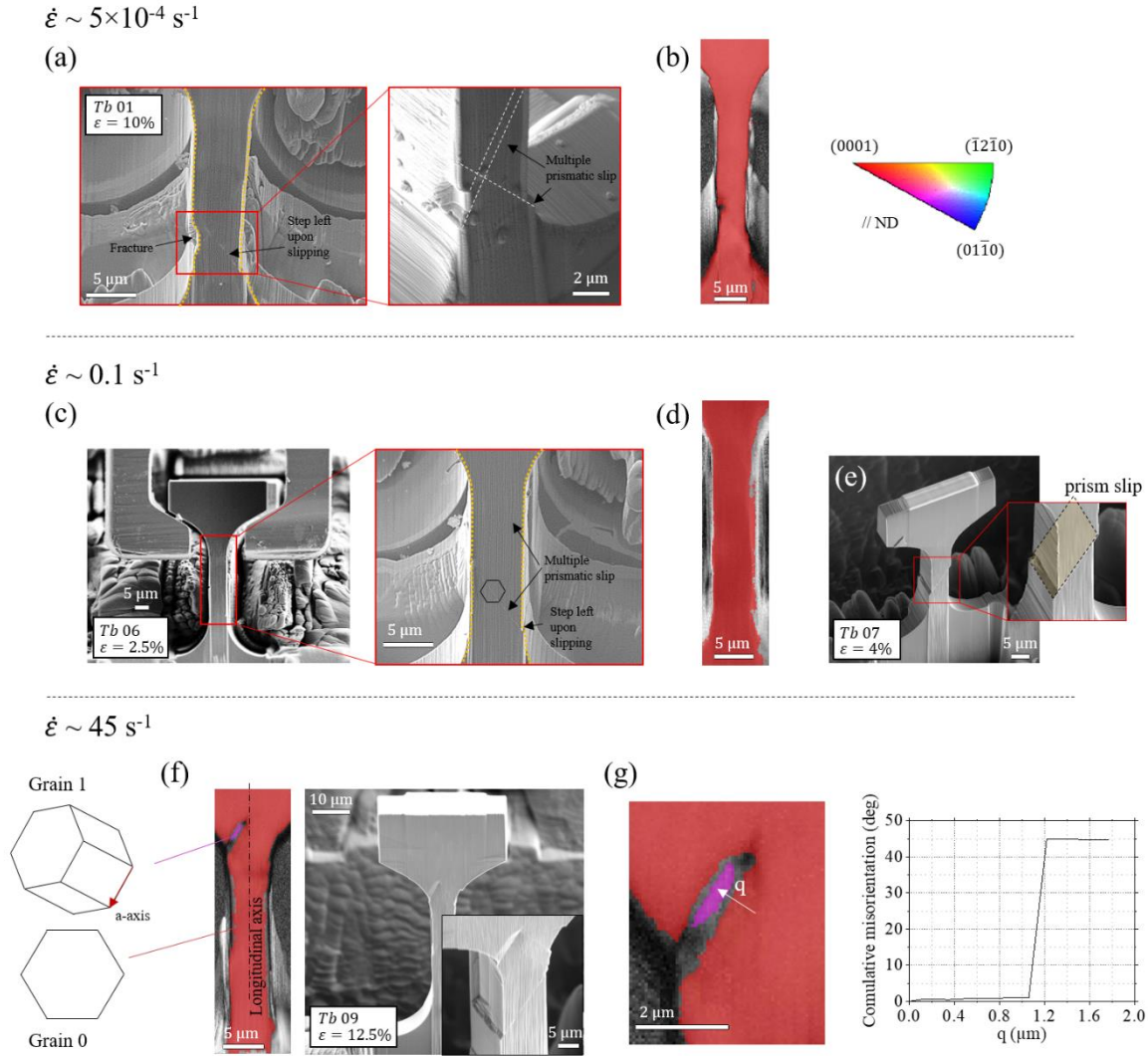


Figure 3: SEM images and EBSD maps illustrating post-mortem deformation features in tensile structures strained at different deformation rates. (a,b) $\dot{\epsilon} = 5 \times 10^{-4} \text{ s}^{-1}$, (c-e) $\dot{\epsilon} = 0.1 \text{ s}^{-1}$, (f,g) $\dot{\epsilon} = 45 \text{ s}^{-1}$. In all the cases, plasticity has been accommodated by prismatic slip, as clearly evincible from the slip traces detected via SEM imaging (a,c,e,f). For $\dot{\epsilon} \leq 0.1 \text{ s}^{-1}$, the EBSD maps (b,d) do not show any twin activity. At the highest applied strain rate, the formation of a new grain $\sim 44^\circ (\pm 1)$ misoriented with respect to the parent crystal around the a-axis has been observed in the location of high stress concentration (indicated with letter "A" in Figure 1) (f,g). The cumulative misorientation is plotted in (g). The IPF colour code refers to the out-of-plane crystal direction (ND).

3.2 [0001] loading (c-axis compression)

In compression, the trend of the stress-strain curve is not characterized by any discrete load drop but rather by continuous plastic flow (Figure 4). The yield stress σ_y has been therefore measured at 0.2% of strain. As for the tensile case, the variation of the τ_{CRSS} with strain rate, from which the *SRS* is derived at yield, is reported in Figure 4e. The calculated values of *SRS*, necessarily associated with pyramidal slip due to the restricting Schmid factor, are ~ 0.015 , ~ 0.042 and ~ 0.131 for low, intermediate and high values of strain rate, respectively, and found to be similar to those reported for prismatic slip. This corresponds to activation volumes V^* of $1.58 \pm 0.1 \text{ nm}^3$, $0.47 \pm 0.08 \text{ nm}^3$ and $0.15 \pm 0.05 \text{ nm}^3$, which, expressed in terms of b^3 (with b the Burgers vector of a $\langle c+a \rangle$ dislocation, $\sim 0.612 \text{ nm}$) would become $\sim 7b^3$, $\sim 2b^3$ and $\sim 0.7b^3$, respectively. Despite the comparable or higher τ_{CRSS} of pyramidal I or II and prismatic slip systems (Table 1), a reduction in the absolute yield values is detected from

c-axis contraction to *c*-axis compression for all the investigated strain rates. This is likely due to the complex tri-axial strain field in the first few-tens of nanometres below the tip-pillar contact surface in compression, which is likely to favour the activation of dislocations at smaller strain levels.

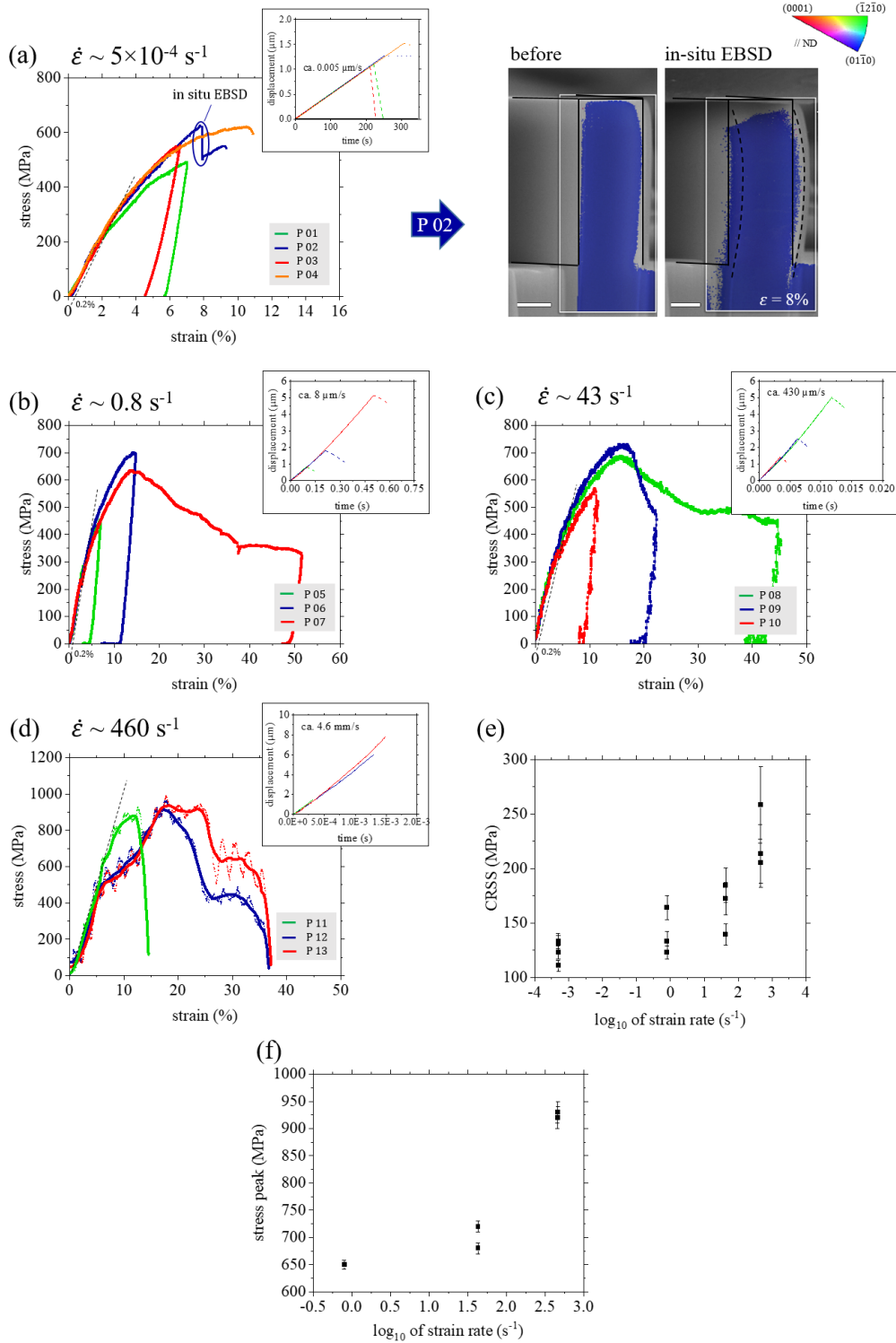


Figure 4: Stress-strain curves for [0001] compression tests at different strain rates: from 5×10^{-4} to 460 s^{-1} (a-d). The inserts illustrate the displacement vs time curves from which the strain rate has been confirmed considering a characteristic height of $10 \text{ }\mu\text{m}$. The variation of the τ_{CRSS} with strain rate is shown in (e). The τ_{CRSS} has been measured at a plastic strain of 0.2% (a-d). Note that the error bars consider also uncertainties ($\pm 100 \text{ nm}$) in the SEM measures of the dimensions of the structures. In (d), the material response is overwhelmed by the oscillation amplitude, not allowing a precise extraction of the material properties.

An adjacent average smoothing procedure every 35 data points has been therefore adopted (note that the experimental sampling rate used for this condition was 1MHz). (f) Maximum nominal stress reached in the structures at different strain rates. All undefined scale bars correspond to 2 μm . The IPF colour code refers to the out-of-plane crystal direction (ND).

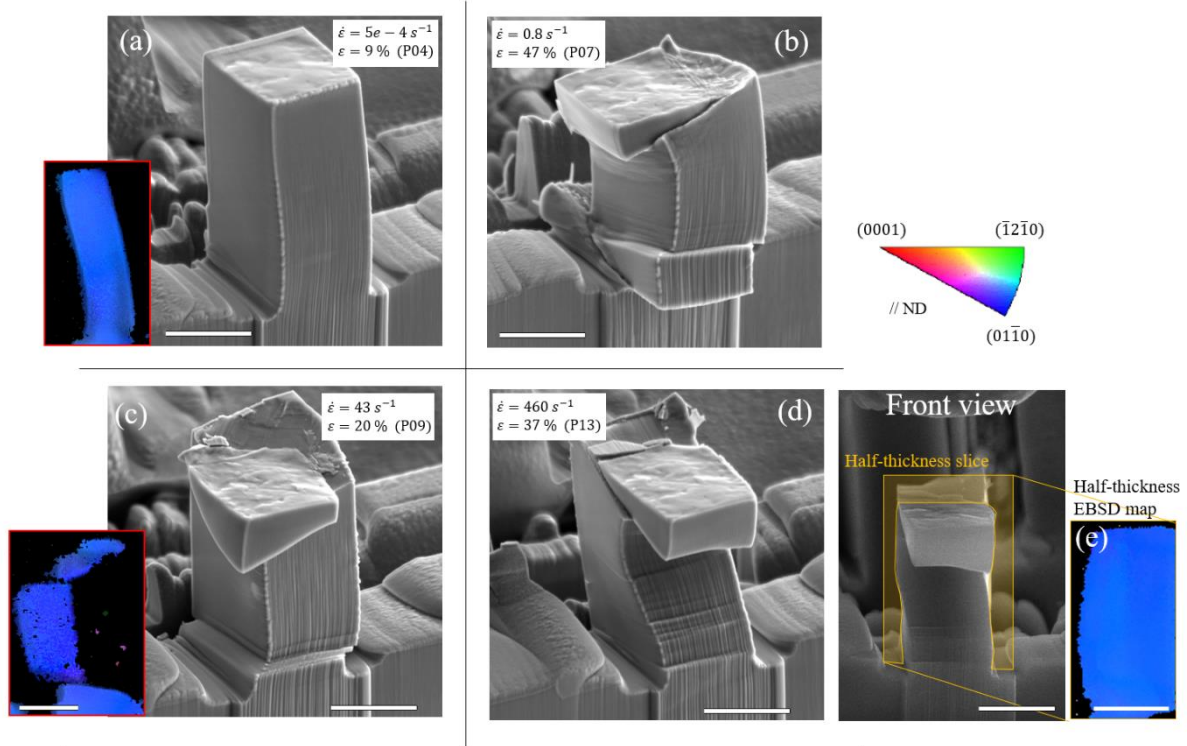


Figure 5: SEM images and EBSD maps for pillars compressed at different strain rates. The pillar number, strain rate and level of strain achieved are indicated in each image (a-d). A bulging mechanism is observed in all structures. A front view SEM image is shown for the pillar compressed at 460 s^{-1} (d). (e) EBSD map taken at half of the thickness of pillar P13 in (d). Plasticity is mainly accommodated by pyramidal and basal slip. No twinning mechanism was detected. All undefined scale bars correspond to 5 μm . The IPF colour code refers to the out-of-plane crystal direction (ND).

At the lowest strain rate ($5 \times 10^{-4} \text{ s}^{-1}$), the setup has been adapted to perform *in situ* HR-EBSD measurements at 8% strain (see Figure 4a-right)) by keeping the flat punch displacement at a constant value while the sample was under load [35,36]. The intermediate map was captured to investigate whether the "lack of CTWs" can be caused by detwinning during unloading. However, no CTW has been detected in loaded conditions. The reduction in stress shown in Figure 4a at $\epsilon = 8\%$ is due to the stress relaxation occurring throughout the holding time (17 minutes) during which the intermediate EBSD map was taken. This relaxation is due to creep of the piezoelectric actuator and the load cell and possibly minor stress relaxation in the material. It is noted that *in situ* EBSD acquisition was not possible for the other applied strain rates as the total testing time was less than 1s (inserts in Figure 4b-d). In Figure 4 it can also be seen that, regardless of the imposed strain rate, a stress peak is reached at around 20% strain after which a lower load is required for further straining (softening). The magnitude of the stress peak however changes with strain rate, as reported in Figure 4f, reaching $\sim 900 \text{ MPa}$ at 460 s^{-1} . Thus, Figure 4f illustrates the maximum load that a 5 μm -sized pillar (with a 2:1 height-width aspect ratio) can support during [0001] compression before ceding at different strain rates. In some cases, the misalignment between the *c*-axis and loading direction, induced by the instability of the structure, allows basal slip activity (see Figure 5). Despite the appearance of cleavage planes, indicative of the typical fragile nature of Mg at large strains (Figure 5), a remarkable resistance

to applied load occurs at the microscale even at HSRs for strain levels below $\sim 20\%$. After testing, post-mortem EBSD maps were acquired on the front surface of each pillar without revealing the presence of CTWs or "anomalous" new grains (not relatable to well-known twinning modes). However, to investigate their possible presence inside the pillar structures, subsequent EBSD maps have been acquired through the thickness of the pillars by FIB tomography. Again, no new twin/grain formation was revealed for structures with gauge cross-section dimensions of $5 \times 5 \mu\text{m}^2$ and aspect ratio 2:1, as also reported elsewhere [4–6].

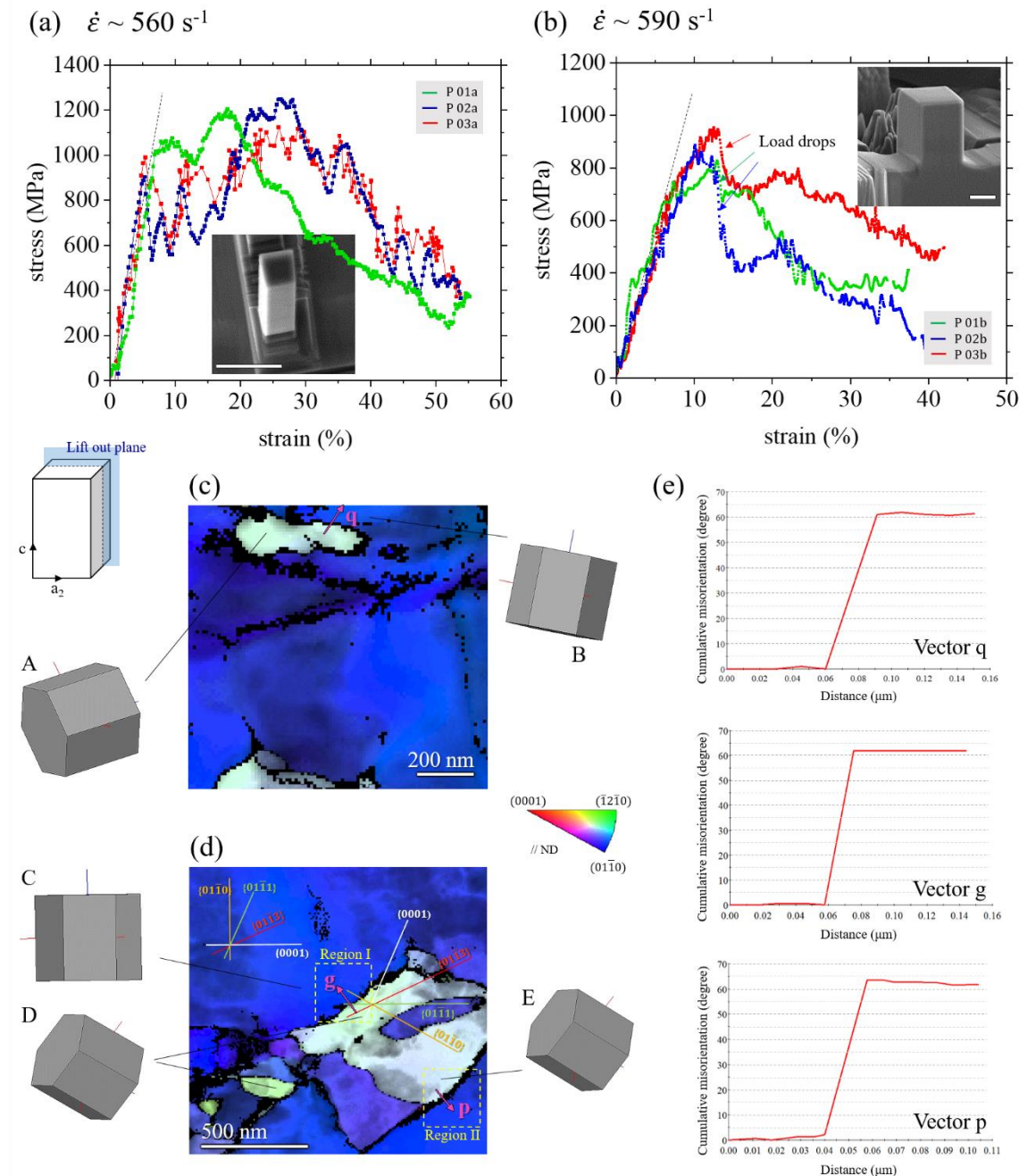


Figure 6: Stress-strain curves and SPED orientation maps of [0001] shock-compressed pillars of different dimensions and aspect ratios: (a) $1.2 \times 1.2 \mu\text{m}^2$ (2:1 aspect ratio), (b) $5 \times 5 \mu\text{m}^2$ (3:2 aspect ratio). SEM images embedded in the graphs illustrate undeformed structures. Scale bars: $2 \mu\text{m}$. (c,d) Orientation maps obtained via SPED illustrating the formation of new grains in (c) $1.2 \times 1.2 \mu\text{m}^2$ (2:1 aspect ratio), and (d) $5 \times 5 \mu\text{m}^2$ (3:2 aspect ratio) pillars. The reliability index in the maps is greater than

20%, above the acceptability threshold. A graphic representation of the crystal orientations is reported to facilitate the visualization. The lift out plane is illustrated (the reference system corresponds to that of Figure 1d). In (d), the (0001) -in white-, $\{10\bar{1}3\}$ -in red-, $\{10\bar{1}1\}$ -in green-, and $\{10\bar{1}0\}$ -in orange- traces are highlighted within the parent and the new grain. (e) Cumulative misorientation profiles along the vectors indicated with q , g and p in (c,d). The new grains are characterized by a $\sim 62^\circ$ misorientation around the a -axis with respect to the initial crystal. The IPF colour code refers to the out-of-plane crystal direction (ND).

Nevertheless, the nucleation of new grains was observed in pillars with smaller dimensions and aspect ratios. In particular, to reach higher stress levels for a given strain value, with the intent of triggering CTW or new grains formation, different pillar dimensions have been chosen and tested at HSR. Figure 6 shows the stress-strain curves, pre- and post-deformation SEM images and SPED maps of $1.2 \times 1.2 \mu\text{m}^2$ (aspect ratio 2:1) and $5 \times 5 \mu\text{m}^2$ (aspect ratio 3:2) pillars. The smaller pillars ($1.2 \times 1.2 \mu\text{m}^2$) have been deformed up to $\sim 50\%$ strain with the τ_{CRSS} increasing to ~ 1 GPa ("smaller is stronger", Figure 6a, [37–39]), which is twice as high as what was measured for the $5 \times 5 \mu\text{m}^2$ pillars (Figure 4). Using SPED it can be observed that new small grains have formed (Figure 6c), but with characteristics that do not correspond to well-known twin modes. Similar to the increase in stress level achieved by decreasing the characteristic dimension (width) of the pillar, a reduction in the aspect ratio of the structure from 2:1 to 3:2 (while keeping same reference dimensions: $5 \times 5 \mu\text{m}^2$) also affects the plasticity mechanism and the nominal stress level reached (Figure 6b). Indeed, new grains have been observed (Figure 6d). With respect to their crystallographic nature, the parent-new grain misorientations correspond to $\sim 62^\circ$ around the a -axis. The *in situ* videos of compression tests carried out at the highest applied strain rates can be found in Supplementary Video 2, 3 and 4.

4. Discussion

In tension (c -axis contraction), the activation of prismatic slip systems promotes the relative movement above and below the slip planes (Figure 3e, Tb05) that results in (i) a stress plateau representing the constant friction stress required for continuous gliding (Figure 2a-c) and (ii) limited further plasticity compared to that observed in c -axis compression, for all the applied strain rates. Indeed, in the case of c -axis compression, the symmetry of the crystal with respect to the loading axis leads to twelve (six for $\{10\bar{1}1\}$ and six for $\{2\bar{1}\bar{1}2\}$) equivalently stressed pyramidal slip systems, which accommodate plastic deformation and promote the strong hardening observed in Figure 4 up to 20% of strain. Nevertheless, in both cases the absence of twinning significantly reduces the ductility of Mg during c -axis compression and especially c -axis contraction. This is in contrast to c -axis extension experiments where DT represents the predominant mechanism that accommodates plastic deformation, allowing the material to withstand a large amounts of strain without cracking even at HSRs [40,41].

4.1 c -axis contraction: the case of the reoriented (44° , a -axis) grain

CTW or TTW do not contribute to accommodating plastic deformation in Mg during c -axis contraction. However, the nucleation of a new grain in Figure 3f,g is observed and is likely induced by the high stress level achieved in the region indicated with letter "A" in the insert of Figure 1a. "A" represents, due to the geometry of the structure, the area of higher (triaxial) stress concentration. Therefore, complex and higher strain fields can be perceived at

the atomic scale, favouring the activation of equally complex deformation modes, especially upon exhaustion of dislocation-mediated plasticity. Although the nucleation of the new grain shown in Figure 3f,g most likely occurred at high strain level and is therefore of very limited relevance to the mechanism of accommodation of the large imposed deformation (especially in relation to its limited spatial evolution), it is nevertheless interesting to delve into its crystallographic characteristics. In particular, the 44° matrix-new grain misorientation relationship between Grain 0 and Grain 1 (Figure 3f,g) cannot be classified in terms of a known twinning system, predicted by the crystallographic shear-based theory of twinning [18] (Table 1). Other possibilities must therefore be considered.

Table 2: Twin type and corresponding misorientation angle observed experimentally in the Mg crystal [2,30,42–46].

<i>Type of twin</i>	<i>Misorientation angle/axis</i>
$\{10\bar{1}1\}$	$56.2^\circ \langle \bar{1}2\bar{1}0 \rangle$
$\{10\bar{1}2\}$	$86.3^\circ \langle \bar{1}2\bar{1}0 \rangle$
$\{10\bar{1}3\}$	$64^\circ \langle \bar{1}2\bar{1}0 \rangle$
$\{10\bar{1}4\}$	$53^\circ \langle \bar{1}2\bar{1}0 \rangle$
$\{30\bar{3}2\}$	$39.2^\circ \langle \bar{1}2\bar{1}0 \rangle$
$\{30\bar{3}4\}$	$70.8^\circ \langle \bar{1}2\bar{1}0 \rangle$
$\{10\bar{1}1\}$ - $\{10\bar{1}2\}$	$37.5^\circ \langle \bar{1}2\bar{1}0 \rangle$
$\{10\bar{1}1\}$ - $\{10\bar{1}2\}$	$30.1^\circ \langle \bar{1}2\bar{1}0 \rangle$
$\{10\bar{1}1\}$ - $\{10\bar{1}2\}$	$66.5^\circ \langle \bar{5}9\bar{4}3 \rangle$
$\{10\bar{1}1\}$ - $\{10\bar{1}2\}$	$69.9^\circ \langle \bar{2}4\bar{2}1 \rangle$
$\{10\bar{1}2\}$ - $\{10\bar{1}2\}$	$7.4^\circ \langle \bar{1}2\bar{1}0 \rangle$
$\{10\bar{1}2\}$ - $\{10\bar{1}2\}$	$59.9^\circ \langle 10\bar{1}0 \rangle$
$\{10\bar{1}2\}$ - $\{10\bar{1}2\}$	$60.4^\circ \langle \bar{8}1\bar{7}0 \rangle$
$\{10\bar{1}2\}$ - $\{10\bar{1}2\}$	$22.2^\circ \langle \bar{1}2\bar{1}0 \rangle$

It is to note that other matrix \rightarrow new grain transformations not correspondent to well-known twin systems have been recently observed. In particular, at high stress levels induced by either reducing the specimen size or under higher strain rate loading, a pyramidal I to basal plane transformation was reported to take place during [0001] compressions of Mg nanopillars [17], similarly to the prismatic to basal plane transformation that originates during $[10\bar{1}0]$ compression [41,47–49], suggesting that also a deformation-induced plane transformation (unit cell reconstruction) has likely taken place in region A of Tb09 (Figure 1a and Figure 3f) under high loading rates. However, it is difficult to understand the precise mechanism that governed its nucleation. Contrary to the strain field exerted on the crystalline structure under c -axis compression (expansion along the axes perpendicular to the c -axis), the strain field in c -axis contraction reduces the crystallographic a -axis compatibly to the orientation of the crystal relative to the loading direction (Figure 1b). The atomic displacements corresponding to the mechanical loading are hence different to those in [0001] and $[10\bar{1}0]$ compressions, and thus the prismatic to basal and pyramidal I to basal plane transformations cannot explain the (44° , a -axis) misorientation observed here.

Without restricting the investigation to classical twinning modes predicted by the crystallographic theory of twinning, to mathematically correlate the reorientation process of a crystal from an initial (matrix) m to a new n configuration, three matrices can be used [15]: the distortion matrix \mathbf{F} , the coordinate transformation matrix \mathbf{T} , and the correspondence matrix \mathbf{C} , with $\mathbf{C} = \mathbf{T} \mathbf{F}$ (see Appendix A). Contrary to what is computed for deformation

twinning, solutions that require the breakdown of the invariant plane strain condition were also considered here, which correlate the lattice of the matrix and the lattice of the new grain not necessarily by the same crystallographic plane (same Miller indices) or by two equivalent planes of the same family. This employs the concept of *weak twinning*. In relation to this, a possible solution emerged, for which the initial lattice is restored in a 43.1° reoriented new configuration around the a -axis (close to the 44° detected with EBSD). This (43.1° , a -axis) is given by:

$$\mathbf{F}_{hex} = \begin{pmatrix} 1 & 0.1235 & -0.6523 \\ 0 & 0.9135 & 0.3618 \\ 0 & 0 & 1.0945 \end{pmatrix} \quad (2)$$

$$\mathbf{T}_{hex}^{n \rightarrow m} = \begin{pmatrix} 1 & -0.1351 & 0.6407 \\ 0 & 0.7296 & 1.2814 \\ 0 & -0.3648 & 0.7296 \end{pmatrix} \quad (3)$$

from which

$$\mathbf{C}_{hex}^{n \rightarrow m} = \mathbf{T}_{hex}^{n \rightarrow m} \mathbf{F}_{hex} = \begin{pmatrix} 1 & 0 & 0 \\ 0 & 2/3 & 5/3 \\ 0 & -1/3 & 2/3 \end{pmatrix} \quad (4)$$

Details of this calculation are given in Appendix B. Concerning the solution found, using Eq. (4) and Eq. (A.2) (Appendix A.1), the $(0\bar{1}12)_m$ plane ($(0\bar{1}2)$ in the 3-index notation) is transformed into the $(0003)_n$ plane (i.e. (001)). Accordingly, Grain 0 and Grain 1 (Figure 3f) can be related by a $(0\bar{1}12)_m // (0001)_n$ *weak interface* (Figure 7b-c). It is important to note that the trace of the interface experimentally observed (Figure 3g) indeed follows the dashed line reported in Figure 8b. The relative pole figures shown in Figure 8a-b confirm the overlapping stereographic projections between the selected plane combinations. The 43.1° misorientation around the $[\bar{2}110]$ axis (or a -axis) can be checked using the matrix of coordinate transformation between the parent and the new grain bases (Appendix A.3).

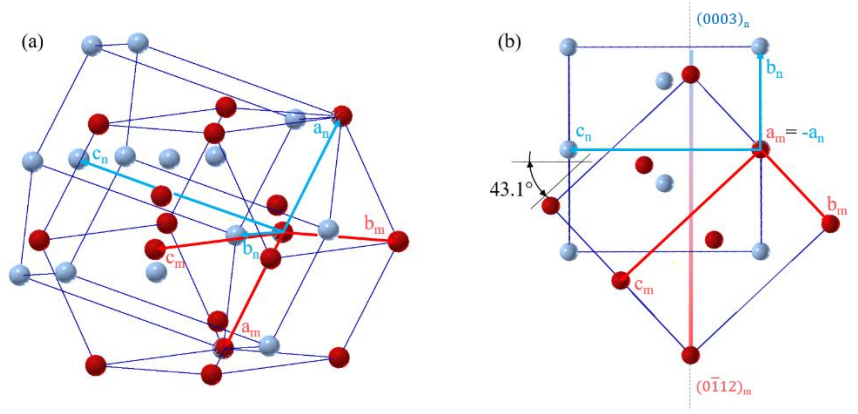


Figure 7: Schematic representing the orientation relations between the parent and new grain crystals for the solution found in correspondence to the observed new grain formation in region A in Figure 1a. (a) 43.1° misoriented parent (m , blue coloured) and new grain (n , red coloured) crystals around the a -axis. (b,c) $(0\bar{1}12)_m \rightarrow (0001)_n$ plane transformation. (b) represents the projection of the crystals viewed along the normal to the denoted planes.

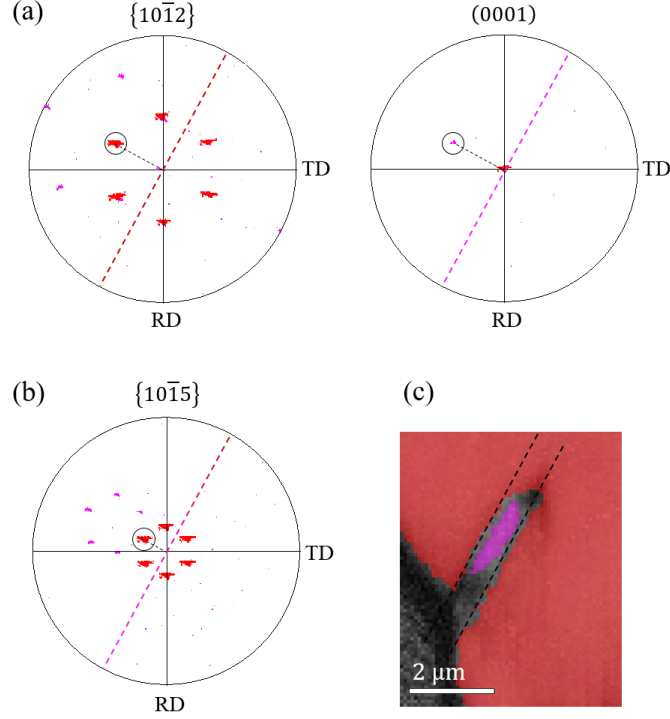


Figure 8: Pole figures of the crystallographic planes that constitute the solution proposed to describe the grain formed in Tb09 (Figure 3f,g). Colours refer to the IPF triangle of Figure 3. The circles identify the overlapping stereographic projections of the normal of the parent and new grain planes that constitute the parent-new grain interface (Figure 3g); the latter denoted with a dashed line. (b) Pole figure associated to the conventional $\{10\bar{1}5\}$ twin. (c) Interface between the initial and reoriented grains (replicated from Figure 3g for reference).

Interestingly, the obtained solution implies that a pyramidal II to basal plane transformation occurred, similarly to the pyramidal I to basal or prismatic to basal transformations reported elsewhere [17,47,48]. The geometric parallelism between the basal plane in the new grain and the $(0\bar{1}\bar{1}2)$ pyramidal plane in the matrix can be indeed observed in Figure 7c and Figure B-1 (Appendix B). Note that for the described parent \rightarrow new grain transformation, the distortion matrix does not correspond to that of a simple shear \mathbf{S} typically used to describe the process of deformation twinning.

4.1.1 The relation between the $(0\bar{1}\bar{1}2)_m \rightarrow (0001)_n$ weak twin and the $\{10\bar{1}5\}$ conventional twin

The rearrangement of atomic positions during the propagation of specific interfaces can be used to explain different grain boundary structures and grain misorientations, as well as the formation of conventional twins [47,50]. In particular, a dual-step mechanism has been reported to govern the formation of TTW in Mg, where the nucleation of the predominant $\{10\bar{1}2\}$ twin is preceded by formation of $\{10\bar{1}1\}_m // (0001)_n$ weak interfaces that establish the lattice correspondence of the twin (90°) with a minor deviation from the ideal orientation (86.3°) [41,47–49]. Additionally, in Ref. [17], even if not specified by the authors, $\{10\bar{1}3\}$ twins and $\{10\bar{1}0\}_m \rightarrow \{10\bar{1}3\}_n$ weak interfaces are observed to form upon the growth of the $\{10\bar{1}1\}_m \rightarrow (0001)_n$ facets. From this, it appears that the prismatic \rightarrow basal and the pyramidal I \rightarrow basal plane transformations, belonging to the new class of deformation mechanism defined as *weak twinning* [22] (that encompasses the concept of *deformation graining*), are at the basis

of the formation of conventional twin modes. Consequently, the pyramidal II \rightarrow basal plane transformation may also represent the initiating mechanism for the evolution of a specific conventional twin.

Using similar arguments as those introduced by Crocker and Bevis [43] to calculate the shear value s from the correspondence matrix in the case of simple shear, Cayron [51] proposed the alternative generalization of s (called "generalized shear", s_g) that continues to work whatever the form of \mathbf{F} (simple shear or not). s_g can be extracted from the distortion matrix \mathbf{F} by

$$s_g^2 = Tr[\mathbf{G}(\mathbf{F} - \mathbf{I})\mathbf{G}^{-1}(\mathbf{F} - \mathbf{I})^T] \quad (5)$$

with \mathbf{G} the metric tensor and \mathbf{I} the 3 \times 3 identity matrix. Eq. (5) is a generalization formula that encompasses the usual shear amplitude for simple shear distortions, and more generally, it allows to quantify the amplitude of any distortion. Other generalization formulae have also been proposed. Similarly to what reported by Bevis and Crocker [52], Cayron [22] introduces the concept of "generalized strain" ε_g , expressed as:

$$\varepsilon_g^2 = Tr[\mathbf{G}\mathbf{F}\mathbf{G}^{-1}\mathbf{F}^T] - N \quad (6)$$

with N the dimension of the space ($N = 2$ in 2D, and $N = 3$ in 3D). (Note that for conventional twins: $s_g = \varepsilon_g = s$). The concept of s_g can be used to justify the formation of basal/prismatic interfaces before $\{10\bar{1}2\}$ twinning, and pyramidal I/basal interfaces before $\{10\bar{1}1\}$ or $\{10\bar{1}3\}$ twinning. In particular, $s_g = 0.092$ for basal/prismatic, $s_g = 0.107$ for pyramidal I/basal, $s_g = 0.130$ for conventional $\{10\bar{1}2\}$ twin mode, and $s_g = 0.137$ for conventional $\{10\bar{1}1\}$ and $\{10\bar{1}3\}$ conventional twin modes. Interestingly, the basal/prismatic *weak twin*, (90° , a -axis), and the conventional $\{10\bar{1}2\}$ twinning mode, (86° , a -axis), have the same value of $\varepsilon_g = 0.130$ and same correspondence matrix [my paper and Cyril's paper]. Analogously, also the pyramidal I/basal *weak twin*, (62° , a -axis), and the conventional $\{10\bar{1}1\}$ or $\{10\bar{1}3\}$ twinning modes, (56° , a -axis) and (64° , a -axis), respectively, have the same value of $\varepsilon_g = 0.137$ and same correspondence matrix (Appendix A.3). For what concerns the case of pyramidal II/basal, (43° , a -axis), of interest here, $s_g = 0.595$ and $\varepsilon_g = 0.608$. Yet, a correlation can also be found between the pyramidal II/basal *weak twin* and a conventional type I twin mode: the $\{10\bar{1}5\}$ twin. Despite thus far never having been reported, it is characterized by a 41° misorientation around the a -axis, with its correspondence matrix exactly that of Eq. (4), as it maintains the $(0\bar{1}15)$ unchanged (see Appendix B), its shear value equal to 0.608, and its plane trace follows that of the experimentally observed interface (Figure 8b-c). Indeed, using the mathematical approach adopted in [21,23] for TTW and CTW, the distortion matrix $\mathbf{F}_{hex}^{0\bar{1}15}$ associated to the $\{10\bar{1}5\}$ twin can be derived by applying a small angular correction of 2.1° , as:

$$\mathbf{F}_{hex}^{0\bar{1}15} = \mathbf{R}_{hex}^{2.1^\circ} \mathbf{F}_{hex} = \begin{pmatrix} 1 & 0.1235 & -0.6523 \\ 0 & 0.9129 & 0.4027 \\ 0 & -0.0343 & 1.0801 \end{pmatrix} \quad (7)$$

Differently to \mathbf{F} , $\mathbf{F}_{hex}^{0\bar{1}15}$ is a shear matrix. The set of eigenvalues is reduced to $\{1\}$ and its eigenspace is of dimension 2, formed by the vectors $[100]$ and $[051]$ (expressed in the three-index notation), i.e. the $(0\bar{1}5)$ plane. The shear vector, as well as its amplitude, can be determined in the orthonormal basis by:

$$\mathbf{s} = (\mathbf{F}_{ortho}^{0\bar{1}15} - \mathbf{I}) \cdot \mathbf{n}_{ortho} = \begin{pmatrix} -2.59 \\ 1.0715 \\ 0.4515 \end{pmatrix} \quad (8)$$

where \mathbf{n} , expressed in the orthonormal basis in Eq. (8), represents the vector normal to the $(0\bar{1}5)$ plane, i.e.

$$\mathbf{n}_{ortho} = \begin{bmatrix} 0 & -\gamma & 5\frac{\sqrt{3}}{2} \end{bmatrix} \quad (9)$$

with $\gamma = c/a$ (ratio of lattice parameters). The shear amplitude is therefore

$$s = \frac{\|\mathbf{s}\|}{\|\mathbf{n}\|} \approx 0.608 \quad (10)$$

This value of shear is relatively high compared to that required for other possible twinning modes in Mg. Nevertheless, considering that deformation twins in face centered cubic metals, as well as in twinning-induced plasticity steels, are $(111) \langle 112 \rangle$ with a shear amplitude of 0.7, the solution proposed here may be equally realistic. The hcp unit cell reconstruction through pyramidal II to basal plane transformation could be therefore the “sister” of the $\{10\bar{1}5\}$ classical simple shear twin.

Yet, one may question why the pyramidal II/basal plane transformation has taken place compared to all the other possible *weak twins* that require lower generalized shear and strain amplitudes. An answer could be given by analyzing the schematic of the possible vector field of the overall atomic displacements occurring in the case of the $(0\bar{1}12)_m \rightarrow (0001)_n$ transformation. In Figure B-2 (Appendix B), this vector field appears coherent to the strain field perceived by the unit cell at site "A" of the structure in response to the externally applied load (Figure 1a,b). This implies that changes in the locally perceived strain field would limit the evolution of the new grain and could indeed explain why its growth does not cross the longitudinal axis of the T-bar (Figure 3f). This would suggest that the requirement of compatibility between atomic displacements and externally applied strain field plays a significant role in governing the selection of new grains (*weak twins*), as well as their consequent propagation.

4.2 c-axis compression: the case of the reoriented (62° , a -axis) grain

The formation of new grains was also observed in c -axis compression (Figure 6). Here, the parent-new grain misorientations correspond to $\sim 62^\circ$ around the a -axis, recently reported to be produced by the $\{10\bar{1}1\}_m \rightarrow (0001)_n$ (pyramidal I \rightarrow basal) plane transformation [17]. It should be observed that the rarely operative $\{10\bar{1}3\}$ CTW in Mg, predicted by the crystallographic shear-based theory of twinning, is also characterized by a 64° misorientation around the a -axis (see Table 1) [30]. For completeness, Figure 9 reports the pole figures associated to the (0001) , $\{10\bar{1}1\}$ and $\{10\bar{1}3\}$ families of planes. From the prospective of the material response, a large strain burst marks the nucleation of new grains in the nanopillars compressed by Liu et al. [17], in load-controlled testing mode. In displacement-controlled testing mode, employed in the present study, their nucleation likely corresponds to the load drops observed in Figure 6a-b, not observed in Figure 4a-d. Nevertheless, it is important to understand why, during $[0001]$ compressions, the formation of weak twins occurs in submicron-sized [17] rather than micro-sized pillars with aspect ratio of 2:1, or in micro-sized pillars by lowering the aspect ratio.

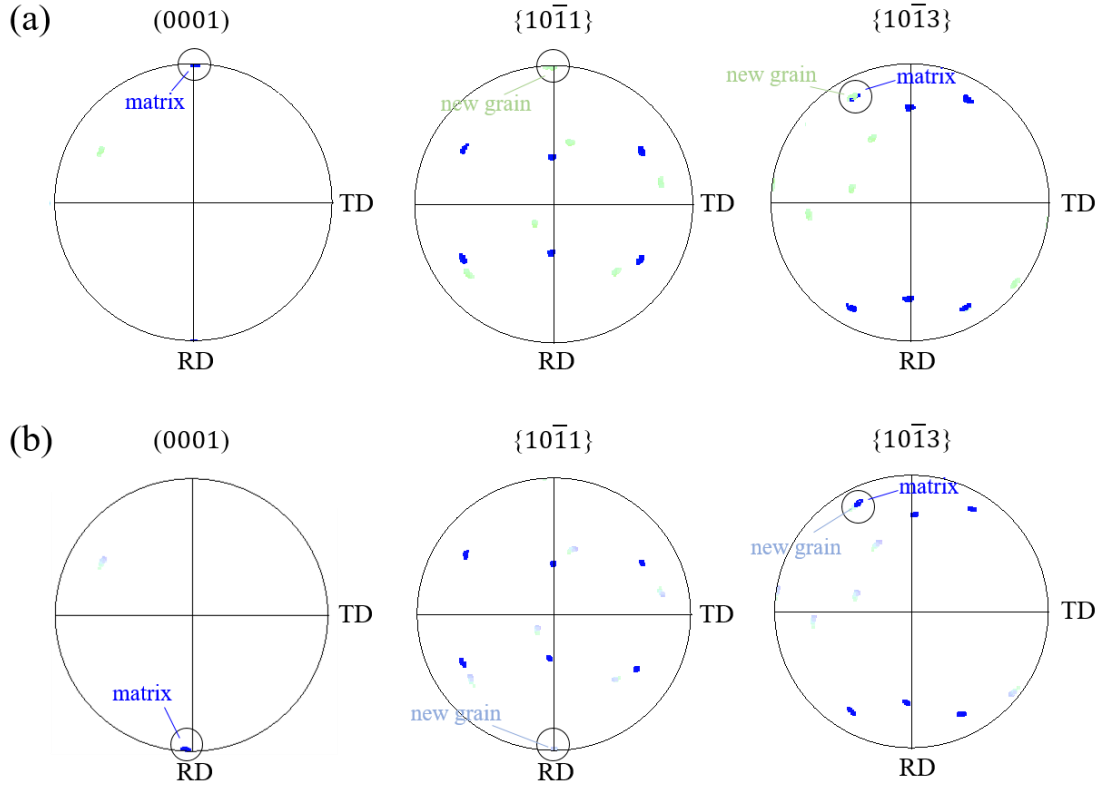


Figure 9: (0001), $\{10\bar{1}1\}$ and $\{10\bar{1}3\}$ pole figures illustrating the two different solutions that can describe the character of the parent-new grain interfaces formed in [0001] compressed micropillars (Figure 6c,d). Colours refer to the invers pole figure of Figure 6. The pole figures in (a) are taken from the sub-region I shown in Figure 6d whilst those in (b) from sub-region II. The circles identify the overlapping stereographic projections of the normal of the parent and new grain planes that constitute the parent-new grain interface.

4.2.1 Smaller pillar cross-section, same aspect ratio

The formation of new grains in smaller pillars can be explained in terms of size-dependent plasticity [53,54]. In contrast to the occurrence of massive shearing produced by single deformation slip crossing the entire structure, single-ended source length dislocations form in pillars of smaller volumes as a result of truncation of dislocation source operation by free surfaces and justify the sample size effect on the measured flow stress of microcrystals [53]. In particular, below a critical size, the statistical averaged distance between the dislocation pin and the free surface becomes too small that requires higher force to operate pre-existing dislocations via Orowan bowing mechanism [55], eventually leading to the conversion from propagation to nucleation-limited dislocation mechanism. The strain rate-dependent balance between the rate of heterogeneous dislocation nucleation from free surfaces and the rate of dislocation escape at free surfaces (before being able to multiply), defines the dislocation density within the pillar volume during the deformation. The plastic flow thus differs from the continuous strain hardening of bulk crystals, inducing changes in the deformation mechanism behavior. In particular, the material is initially forced to withstand large part of the deformation by thickening the structure along the direction perpendicular to the direction of the load (barrelling). In this regards, in the work of Liu et al. [17] it is indeed clear from *in situ* TEM compressions that all the nanostructures undergo a barreling mechanism throughout the deformation rather than exhibiting the visible sliding along crystallographic slip planes observed in the micro-sized pillars ($5 \times 5 \mu\text{m}^2$ and 2:1 aspect ratio, Figure 4 and Figure 5). In turn, the high multi-axial stress condition that builds up within their

pillars, induces the $(10\bar{1}1)_m \rightarrow (0001)_n$ plane transformation, i.e. the new grain formation. Similarly to that, the high stress levels achieved here by imposing high deformation-rates to $\sim 1.2 \mu\text{m}$ sized pillars (also $\sim 1 \text{ GPa}$ - Figure 6b), kinetically delays the time interval within which the deformation is accepted by shearing along crystallographic slip planes, causing the formation of the detected new grains (Figure 6c). On this basis, it appears that a high stress state represents the necessary requirement to obtain the activation condition for WT (Figure 10). In support of this consideration, also the prismatic \rightarrow basal plane transformation (leading to 90° misoriented grains with respect to the parent crystal around the a -axis) has been reported to occur under high-stress conditions obtained either by reducing the size [48] or by increasing strain rate [41,49].

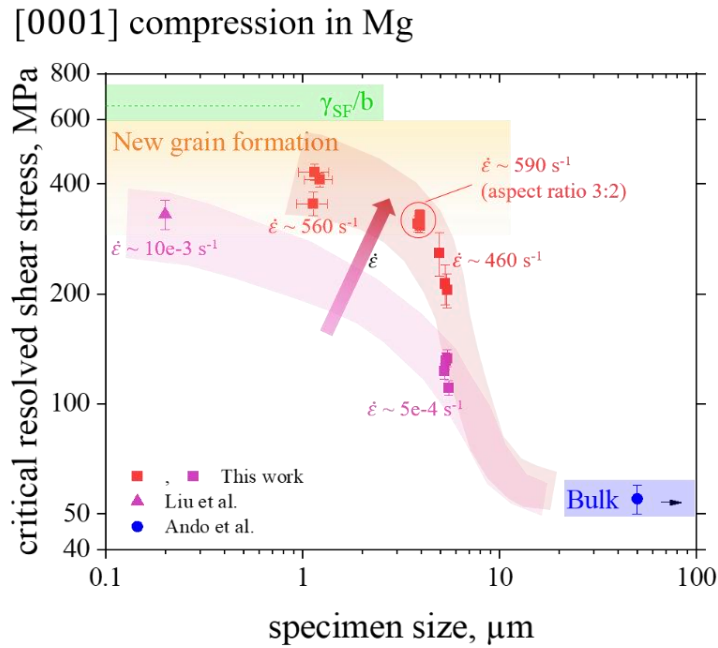


Figure 10: Critical resolved shear stress (calculated at the yield point) of micro-compression samples oriented to deform by pyramidal slip as a function of strain rate and microcrystal diameter. Data refer to pillars with aspect ratio of 2:1, unless specified otherwise. Data point for Liu et al. and Ando et al. are taken from [17,56]. The deformation mechanism map is shown by coloured regions. Note: stacking fault energy of pyramidal slip is considered ca. $425 \pm 25 \text{ mJ m}^{-2}$ from [57]; $b_{\langle c+a \rangle} = 0.612 \text{ nm}$.

4.2.2 Same pillar cross-section, smaller aspect ratio

A reduction in the aspect ratio of the structure from 2:1 to 3:2 (while keeping same dimensions: $5 \times 5 \mu\text{m}^2$) has also been observed to induce the formation of new grains (Figure 6b,d). The main effect of reducing the aspect ratio resides in the change of the geometrical constraints exerted by the surrounding material that yield a deformation behaviour for which the material is forced to barrel. In other words, the initial barreling-induced high multi-axial deformation state may be caused by the geometrical impossibility for the preferable deformation slip mode to cross the structure from one side to the other (Figure 11a). Indeed, setting $(90-\theta)$ the angle between the loading direction and the slip plane with the highest Schmid factor, it is reasonable that barreling is favored in structures with aspect ratio $< \tan(\theta)$, limiting the rate of dislocation escape by crossing the structure with consequent development of high internal stresses and dislocation density. In addition to that, by reducing the aspect ratio, the diagonal shear bands that form at the corners of the pillar intersect at the core of the structure and further produce a high local strain that results in a bimodal strain distribution in the plane normal to the loading direction; in such case, the

triaxial stress state usually formed below the pillar top surface (dead zone) and the uniform strain usually developed in the core are connected by a high strain gradient [58], promoting the occurrence of complex deformation mechanisms. Along this line, Sim et al. [59] report molecular dynamic (MD) simulations that reveal the evolution of the deformation microstructure in Mg pillars of different aspect ratios oriented with the $[2\bar{1}10]$ direction parallel to the loading direction (Figure 11b). In their work, even if not clearly addressed, the decrease in aspect ratio to 1:2 (height vs width) leads to the impossibility of prismatic slip to cross the structure, causing a higher amount of dislocations to remain confined within the pillar volume with a subsequent formation of a new grain 90° misoriented with respect to the parent crystal. Such formation of a new grain was not observed in their work in structures with higher aspect ratio, and can be extended to the present work.

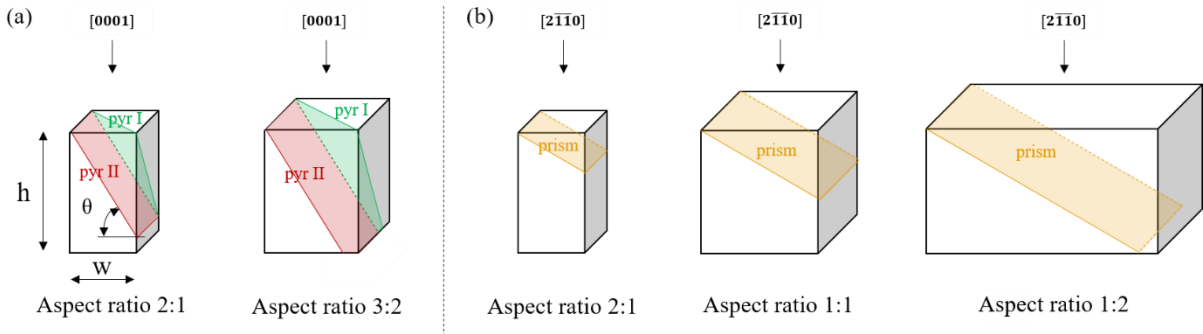


Figure 11: Schematic of the geometrical relationships between the traces of the active slip modes and the pillar aspect ratio during (a) $[0001]$ and (b) $[2\bar{1}10]$ compressions. The impossibility for the preferable deformation slip mode to cross the structure from one side to the other occurs in structures where the aspect ratio becomes lower than $\tan(\theta)$. θ is defined as the angle between the sliding plane and the horizontal plane.

5. Summary and Conclusions

In this work, the mechanical response of pure magnesium under c -axis compression and contraction has been investigated at the microscale, extending the currently published results to high strain rate deformations. In line with what was observed elsewhere [4–6], the accommodation of the plastic deformation occurs predominantly by pyramidal and prismatic slip during c -axis compression and contraction, respectively. The strain rate sensitivities associated to these deformation modes were found to be similar and in the range from 0.01 to 0.131. The increase in the stress induced by the increase in strain rate, however, has not triggered the activation of CTW within the testpieces in both the loading modes. Nevertheless, new grains have been detected, whose crystallographic characteristic cannot be attributed to any conventional twin mode predicted by the classical shear-based theory of twinning. To raise awareness of the relevance of the experimental observation of new grains, it is worth to remind that several other works report "anomalous" twinning characteristics [10,20,60] such as twins whose habit planes are not invariant. As any theory should be judged by its predictions, the increasing number of experimental evidences of unusual misorientation relationships that cannot be related to known twinning systems suggests that the formation of new grains in Mg, and the mechanism governing the incubation period of an embryonic twin, cannot be treated through the shear-based theory of twinning (i.e. distortion matrix being a shear matrix). The concept of *weak twinning* introduced by Cayron [22], was therefore adopted in this work, in which the parent-new grain interface is not anymore necessarily fully invariant as for usual deformation twinning, but can be slightly distorted

to be transformed into a new non-equivalent plane. This approach revisits the list of possible lattice transformations and allowed to identify a pyramidal II to basal plane transformation during c-axis contraction for which the required field of atomic displacements appears pertinent to the strain field perceived by the material at the nucleation site. Grains with crystallographic features suggesting a mechanism of unit cell reconstruction through the transformation from pyramidal I to basal plane were also observed in c-axis compression, in line with recent published work [17]. Nevertheless, the increase in pillar size and in aspect ratio seems to disfavour the formation of new grains. As the new grain formation represents an alternative to cracking, the choice of the pillar size in microsamples may represent a strategy to adapt the plasticity for a given strain level, enhancing the ductility of Mg. However, due to the high stress level required for new grain formation in these loading conditions, it can be questioned in which extent this mechanism can be applied in bulk Mg. High stress conditions can be achieved at the GBs, vicinity of precipitates, and dislocation pile-ups, suggesting that it can be detected in bulk polycrystalline samples. However, it cannot be generalized as a main mechanism of deformation as it requires exceptionally high stresses and specific strain fields for a precise crystallographic orientation, and the material may likely fail before new grain formation occurs.

CRedit authorship contribution statement

N.M.d.V.: Conceptualization, Methodology, Validation, Investigation, Data curation, Writing. **A.S.:** Methodology, Validation, Investigation, Writing- review & editing. **C.C.:** Computer calculation, Validation, Investigation, Writing - review & editing. **S.K.:** Methodology, Investigation, Writing - review & editing. **T.E.J.E.:** Methodology, Investigation, Writing - review & editing. **C.P.:** Methodology, Investigation. **M.J.:** Methodology, Investigation. **J.T.P.:** Methodology, Writing - review & editing. **R.L.:** Project administration, Writing - review & editing. **J.M.:** Conceptualization, Resources, Investigation, Project administration, Validation, Writing – review & editing, Supervision. **X.M.:** Conceptualization, Methodology, Project administration, Resources, Investigation, Validation, Writing - review & editing, Supervision.

Acknowledgments

The authors acknowledge financial support from the Swiss National Science Foundation (SNSF project numbers 200021_179011 and 206021_183328). NMDV would like to thank Dr. Daniele Casari for his support and the Scientific Center for Optical and Electron Microscopy ScopeM of the Swiss Federal Institute of Technology ETHZ. SzK was supported by the EMPAPOSTDOCS-II program that has received funding from the European Union's Horizon 2020 research and innovation program under the Marie Skłodowska-Curie grant agreement number 754364. TEJE acknowledges funding from the European Union's Horizon 2020 research and innovation programme under the Marie Skłodowska-Curie grant agreement No. 840222.



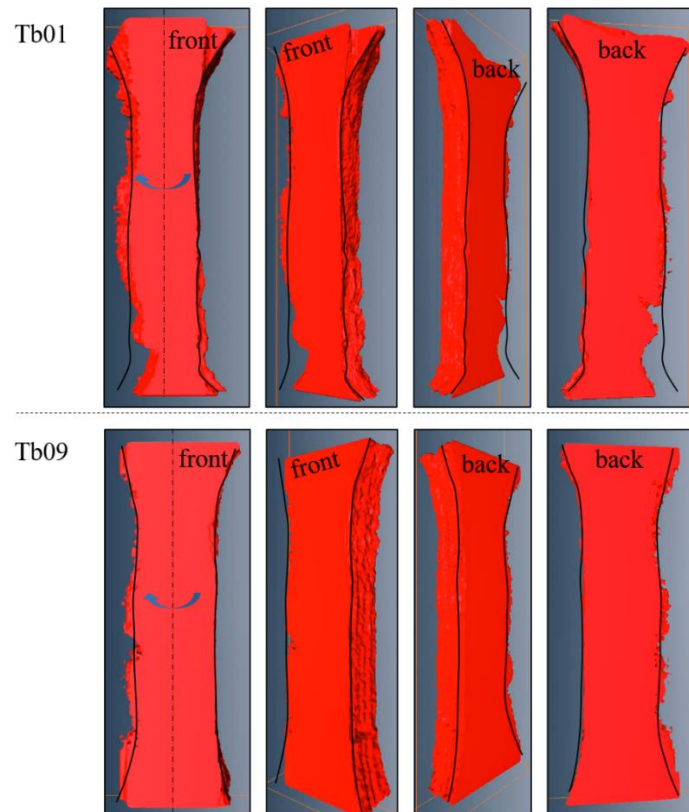
Competing interests

The authors declare no competing interests.

Data availability

The data that support the findings of this study are available from the corresponding author upon reasonable request.

Supplementary Figures:



Supp. Figure S-1: Three-dimensional reconstruction of Tb01 (top) and Tb09 (bottom) deformed at 5×10^{-4} and 45 s^{-1} , respectively. The jagged edges are a result of the uncertainty in EBSD pattern indexation close to the edge of the specimen.

Supplementary Video Legends:

Video 1: Tensile test (c-axis contraction) at 45 s^{-1} .

Video 2: Pillar compression (c-axis compression) at 460 s^{-1} (pillar dimensions: $5 \times 5 \text{ }\mu\text{m}^2$; 2:1 aspect ratio).

Video 3: Pillar compression (c-axis compression) at 560 s^{-1} (pillar dimensions: $1.2 \times 1.2 \text{ }\mu\text{m}^2$; 2:1 aspect ratio).

Video 4: Pillar compression (c-axis compression) at 590 s^{-1} (pillar dimensions: $5 \times 5 \text{ }\mu\text{m}^2$; 3:2 aspect ratio).

Appendices:

A. Transformation matrices

As reported in the main text, to mathematically correlate the reorientation process of a crystal from an initial (matrix) m to a new n configuration, three matrices can be used [15]: the distortion matrix \mathbf{F} , the coordinate transformation matrix \mathbf{T} , and the correspondence matrix \mathbf{C} , with $\mathbf{C} = \mathbf{T} \mathbf{F}$. \mathbf{F} can be calculated in practice considering the vectors of the initial (matrix) basis $(\mathbf{a}_{1m}, \mathbf{a}_{2m}, \mathbf{c}_m)$ transformed by the distortion into new vectors: $\mathbf{a}_{1m} \rightarrow \mathbf{a}'_{1m}$, $\mathbf{a}_{2m} \rightarrow \mathbf{a}'_{2m}$ and $\mathbf{c}_m \rightarrow \mathbf{c}'_m$. In other words, the distortion matrix \mathbf{F} is the matrix formed by the images \mathbf{a}'_{1m} , \mathbf{a}'_{2m} and \mathbf{c}'_m expressed in the initial hexagonal basis (\mathbf{B}_{hex}^m): i.e. $\mathbf{F} = (\mathbf{a}'_{1m}, \mathbf{a}'_{2m}, \mathbf{c}'_m)_{/B_{hex}^m}$. \mathbf{T} is determined from the orientational relationship between the parent and the new reoriented grain, experimentally obtained from the EBSD measurements. The condition that the parent and the new grain have the same volume ensures that \mathbf{F} , \mathbf{T} and \mathbf{C} are unimodular, i.e. have determinants of ± 1 . A further mathematical restriction is that the transformation matrix should fulfil $\mathbf{T} \cdot \mathbf{T}^T = \mathbf{I}$.

A.1 The use of the correspondence matrix

If \mathbf{r} represents a generic vector written in the initial basis (\mathbf{B}_{hex}^m), knowledge of the correspondence matrix $\mathbf{C}_{hex}^{n \rightarrow m}$ is useful to express in the new grain basis (\mathbf{B}_{hex}^n) the coordinates of \mathbf{r}' (i.e. \mathbf{r} after the distortion) as follows:

$$\mathbf{r}'_{/B_{hex}^n} = \mathbf{C}_{hex}^{n \rightarrow m} \mathbf{r}_{/B_{hex}^m} \quad (\text{A.1})$$

Considering \mathbf{r} the vector normal to the crystallographic plane \mathbf{J} (defined by the Miller indices h, k, l , when expressed in the 3-index notation), \mathbf{r}^* in reciprocal space is then a vector whose components are h, k, l . Thus,

$$\mathbf{r}'_{/B_{hex}^n} = (\mathbf{C}_{hex}^{n \rightarrow m})^* \mathbf{r}_{/B_{hex}^m} = (\mathbf{C}_{hex}^{n \rightarrow m})^{-T} \mathbf{r}_{/B_{hex}^m} \quad (\text{A.2})$$

where

$$(\mathbf{C}_{hex}^{n \rightarrow m})^* = (\mathbf{C}_{hex}^{m \rightarrow n})^T \quad (\text{A.3})$$

A.2 The use of the coordinate transformation matrix

It is noted that matrices equivalent to $\mathbf{T}_{hex}^{n \rightarrow m}$ can be obtained by multiplying $\mathbf{T}_{hex}^{n \rightarrow m}$ by the matrices of internal symmetry \mathbf{M} of the hexagonal phase (matrices forming the point group of the hcp phase [61]). For example, in order to determine the rotation matrix $\mathbf{R}_{ortho}^{n \rightarrow m}$ expressed in an initial orthogonal basis (\mathbf{B}_{ortho}^m), which in turn is related to the hexagonal basis (\mathbf{B}_{hex}^m) by

$$\mathbf{H}_{hex} = [\mathbf{B}_{ortho}^m \rightarrow \mathbf{B}_{hex}^m] = \begin{pmatrix} 1 & -\frac{1}{2} & 0 \\ 0 & \frac{\sqrt{3}}{2} & 0 \\ 0 & 0 & \gamma' \end{pmatrix} \quad (\text{A.4})$$

with $\gamma = c/a$ (ratio of lattice parameters), the matrix $\mathbf{T}_{hex}^{n \rightarrow m}$ can be composed with the mirror symmetry \mathbf{M}_{hex} and then be expressed in \mathbf{B}_{ortho}^m . The result will be:

$$\mathbf{R}_{ortho}^{n \rightarrow m} = \mathbf{H}_{hex} \mathbf{M}_{hex} \mathbf{T}_{hex}^{n \rightarrow m} \mathbf{H}_{hex}^{-1} = \begin{pmatrix} -1 & 0 & 0 \\ 0 & 0.7296 & 0.6835 \\ 0 & 0.6839 & -0.7296 \end{pmatrix} \quad (\text{A.5})$$

with

$$\mathbf{M}_{hex} = \begin{pmatrix} -1 & 1 & 0 \\ 0 & 1 & 0 \\ 0 & 0 & -1 \end{pmatrix} \quad (\text{A.6})$$

The matrix $\mathbf{R}_{ortho}^{n \rightarrow m}$ represents a rotation around the a -axis of angle $\cos^{-1}(0.7296) = 43.1^\circ$.

A.3 The correspondence matrix of the $(01\bar{1}1)_m \rightarrow (000\bar{2})_n$ plane transformation and $\{10\bar{1}3\}$ conventional twin

The correspondence matrix associated with the $(01\bar{1}1)_m \rightarrow (000\bar{2})_n$ plane transformation

$$\mathbf{C}_{hex}^{n \rightarrow m} = \begin{pmatrix} 1 & -1/4 & -3/4 \\ 0 & 1/2 & -3/2 \\ 0 & -1/2 & -1/2 \end{pmatrix} \quad (\text{A.7})$$

converts also the $(01\bar{1}3)_m$ into $(01\bar{1}3)_n$ (conventional twin) and $(02\bar{2}0)_m$ into $(01\bar{1}3)_n$.

B. Pyramidal II \rightarrow basal plane transformation: correspondence, distortion and transformation matrices calculation

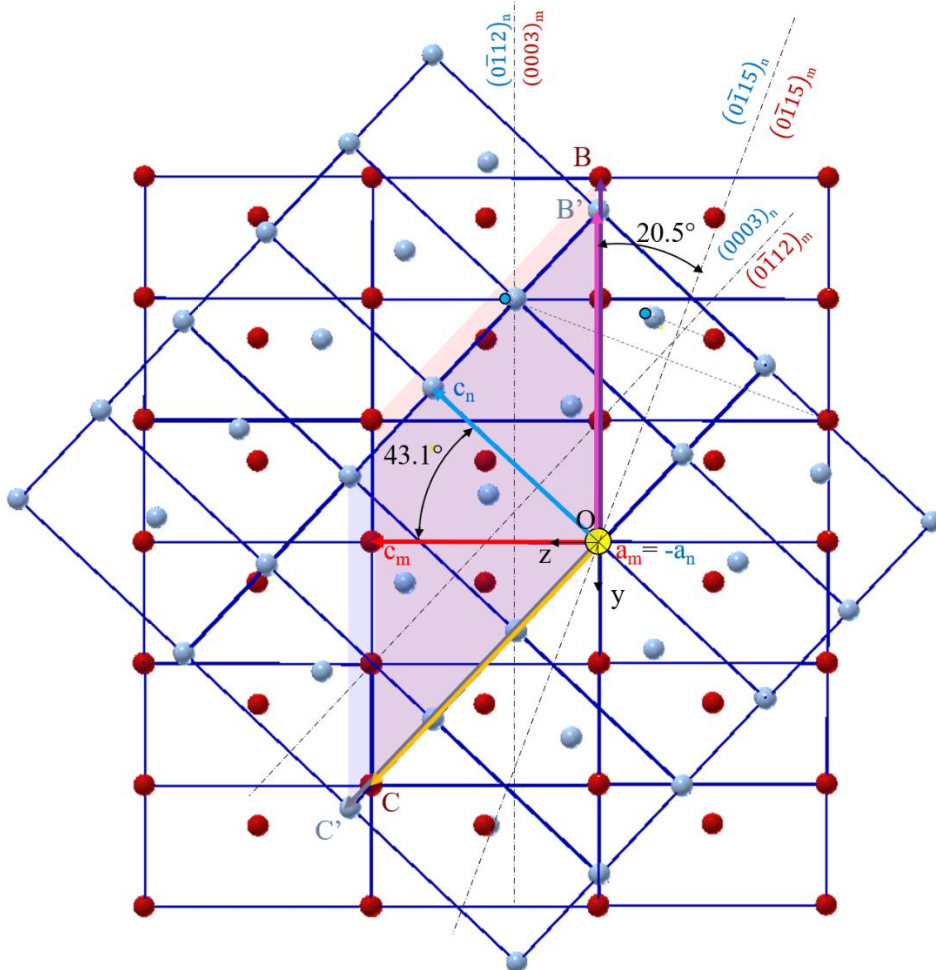


Figure B-1: Model of $(0\bar{1}12) \rightarrow (0003)$ transformation. Series of unit cell repeated periodically and viewed in projection perpendicular to the a -axis. The new grain appears blue, the parent grain in red. The rotation axis is indicated by the yellow coloured circle, representing also the origin of the orthogonal and hexagonal bases. Vectors OA and OB are perpendicular and parallel to the plane of view, respectively. The parent \rightarrow new grain transformation converts the $(0\bar{1}12)_m$ into the $(0003)_n$, and the $(0003)_m$ into the $(0\bar{1}12)_n$. The final configuration is very close to the exact mirror symmetry across the $(0\bar{1}15)$ plane. The atomic positions of the new grain are very close to the positions that would be obtained by mirror symmetry across the $(0\bar{1}15)$ plane, as indicated by the black dashed lines perpendicular to the $(0\bar{1}15)$ plane, as well as by the small blue circles. Atoms in A, B and C, constitute the ABC supercell (transparent red); atoms in A', B', and C', constitute the distorted ABC supercell (transparent blue), i.e. $(ABC)'$.

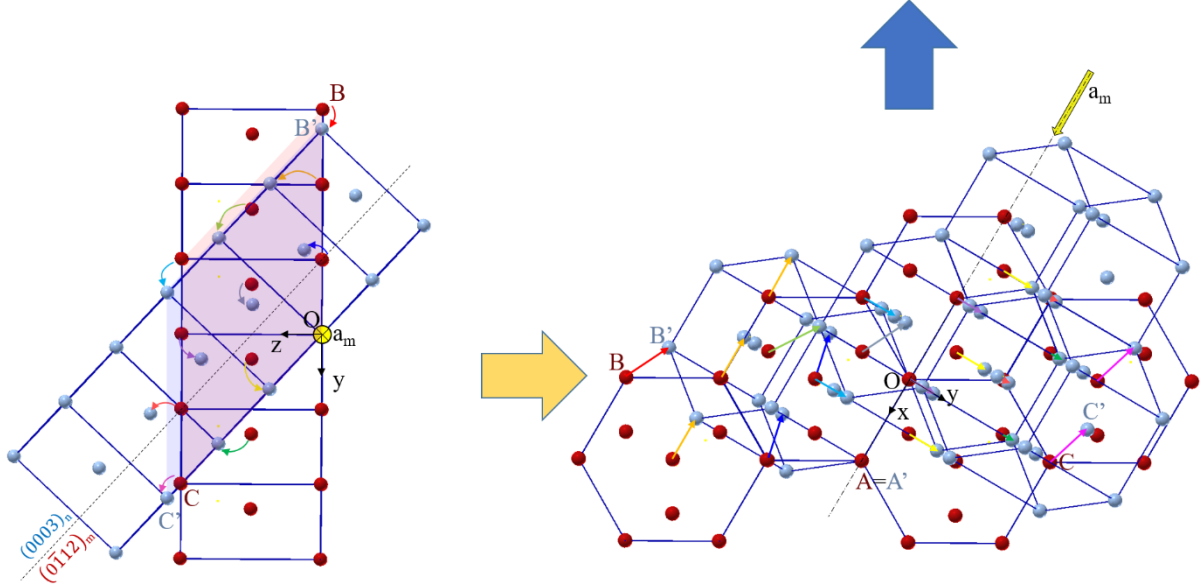


Figure B-2: Proposition of atom displacements for which the $(0\bar{1}12) \rightarrow (0003)$ transformation very close to the exact mirror symmetry across the $(0\bar{1}15)$ plane. For the former, the matrix (red) and new hcp unit cell (blue) have a $43.1^\circ \langle 2\bar{1}10 \rangle$ misorientation; for the latter, they have a $41^\circ \langle 2\bar{1}10 \rangle$ misorientation. The locally perceived strain field in the region "A" of the material (Figure 1a) is indicated by the two bigger arrows on the right-hand side. The vector field of atomic displacements that induces the $(0\bar{1}12)_m \rightarrow (0001)_n$ plane transformation is illustrated by differently coloured arrows. Note that the atomic displacements have almost the same magnitude and are pertinent to the external stress field. The distortion is calculated by considering only the displacements of the atoms in A, B and C, constituting the ABC supercell. It is assumed that their motion causes the subsequent atomic repositioning of the other atoms, similar to a knock-on effect.

We have imagined, after many unproductive attempts, a vector field of atomic displacements that represents the pyramidal II (parent, or matrix m) to basal (new grain, n) plane transformation. Although we cannot ascertain that this model gives the best solution, the solution that emerges provides a series of atomic movements that seem reasonable because are coherent with the strain field perceived in location A (Figure B-1a), they are small and restore the hcp lattice at the end of the process.

We define $\mathbf{B}_{hex} = (a, b, c)$ the usual hexagonal basis and $\mathbf{B}_{ortho} = (x, y, z)$ the orthonormal basis represented in Figure B-1 and linked to \mathbf{B}_{hex} by the coordinate transformation matrix \mathbf{H}_{hex} reported in Eq. (A.4).

The distortion matrix can be calculated by considering an appropriate supercell that conserves the volume at the end of the process. In the present case, the unit cell is ABC (Figure B-1 and Figure B-2). The three column vectors of this cell, OA, OB and OC, form a basis \mathbf{B}_{ABC} given in \mathbf{B}_{ortho} by the coordinate transformation matrix:

$$[\mathbf{B}_{ortho} \rightarrow \mathbf{B}_{ABC}] = \mathbf{B}_{ABC} = \begin{pmatrix} 1 & 3/2 & -1 \\ 0 & -3\frac{\sqrt{3}}{2} & \sqrt{3} \\ 0 & 0 & \gamma \end{pmatrix} \quad (\text{B.1})$$

The three column vectors of the deformed supercell (when the transformation is completed), OA', OB' and OC', form a basis $\mathbf{B}_{(ABC)'}$ given in \mathbf{B}_{ortho} by the coordinate transformation matrix:

$$[\mathbf{B}_{ortho} \rightarrow \mathbf{B}_{(ABC)'}] = \mathbf{B}_{(ABC)'} = \begin{pmatrix} 1 & 1 & -\frac{1}{2} \\ 0 & -2.373 & 1.9066 \\ 0 & 0 & 1.7625 \end{pmatrix} \quad (\text{B.2})$$

The distortion matrix of the process is given in the basis \mathbf{B}_{ortho} by the matrix \mathbf{F}_{ortho} :

$$\mathbf{F}_{ortho} = \mathbf{B}_{(ABC)'}(\mathbf{B}_{ABC})^{-1} = \begin{pmatrix} 1 & 0.1924 & -0.5132 \\ 0 & 0.9136 & 0.1996 \\ 0 & 0 & 1.0945 \end{pmatrix} \quad (\text{B.3})$$

The determinant of the matrix is 1, confirming that the ABC and (ABC)' supercells have the same volume.

This matrix can be expressed in the hexagonal basis \mathbf{B}_{hex} by using the formula of coordinate change:

$$\mathbf{F}_{hex} = (\mathbf{H}_{hex})^{-1}\mathbf{F}_{ortho}\mathbf{H}_{hex} = \begin{pmatrix} 1 & 0.1235 & -0.6523 \\ 0 & 0.9135 & 0.3618 \\ 0 & 0 & 1.0945 \end{pmatrix} \quad (\text{B.4})$$

which reflects that of Eq. (2). Note that the displacement field is given by:

$$\mathbf{x}'_{/\mathbf{B}_{hex}^m} - \mathbf{x}_{/\mathbf{B}_{hex}^m} = (\mathbf{F}_{hex} - \mathbf{I}) \cdot \mathbf{x}_{/\mathbf{B}_{hex}^m} \quad (\text{B.5})$$

where \mathbf{x} is a vector of the parent basis that defines the initial atomic positions, and \mathbf{x}' is the image of a vector \mathbf{x} obtained by a linear distortion: $\mathbf{x}'_{/\mathbf{B}_{hex}^m} = \mathbf{F}_{hex} \cdot \mathbf{x}_{/\mathbf{B}_{hex}^m}$.

Despite \mathbf{F}_{hex} is calculated by considering only the displacements of the atoms in A, B and C, it is assumed that their motion causes the subsequent atomic repositioning of the other atoms, similar to a knock-on effect.

The correspondence matrix, nevertheless, can be calculated by considering the vectors used to build the ABC cell:

$$\begin{aligned} \mathbf{OA} : \mathbf{a}_m &\rightarrow \mathbf{OA}' : \mathbf{a}'_m = -\mathbf{a}_n \\ \mathbf{OB} : -3\mathbf{b}_m &\rightarrow \mathbf{OB}' : -3\mathbf{b}'_m = 2\mathbf{b}_n + \mathbf{c}_n \\ \mathbf{OC} : 2\mathbf{b}_m + \mathbf{c}_m &\rightarrow \mathbf{OC}' : (2\mathbf{b}_m + \mathbf{c}_m)' = -3\mathbf{b}_n \end{aligned} \quad (\text{B.6})$$

where: \mathbf{a}_m is along x , \mathbf{b}_m along $y - \frac{1}{2}x$, and \mathbf{c}_m along z .

This means that the basis \mathbf{B}_{ABC}^m formed by the three vectors \mathbf{a}_m , $-3\mathbf{b}_m$, and $2\mathbf{b}_m + \mathbf{c}_m$, written as a column, is transformed by distortion into a matrix formed by three new vectors equal to $-\mathbf{a}_n$, $2\mathbf{b}_n + \mathbf{c}_n$, and $-3\mathbf{b}_n$, of the twinned crystal. They form a new basis noted $\mathbf{B}_{(ABC)'}^n$. The negative sign of $-\mathbf{a}_n$ is a direct consequent of having imposed the condition that both have a positive determinant. The basis \mathbf{B}_{ABC}^m expressed in the parent basis $\mathbf{B}_{hex}^m = (\mathbf{a}_m, \mathbf{b}_m, \mathbf{c}_m)$ and the basis $\mathbf{B}_{(ABC)'}^n$ expressed in the new grain basis $\mathbf{B}_{hex}^n = (\mathbf{a}_n, \mathbf{b}_n, \mathbf{c}_n)$ are, respectively, given by:

$$\mathbf{B}_{ABC}^m = \begin{pmatrix} 1 & 0 & 0 \\ 0 & -3 & 2 \\ 0 & 0 & 1 \end{pmatrix} \quad (\text{B.7})$$

$$\mathbf{B}_{(ABC)'}^n = \begin{pmatrix} -1 & 0 & 0 \\ 0 & 2 & -3 \\ 0 & 1 & 0 \end{pmatrix} \quad (\text{B.8})$$

$\mathbf{T}_{hex}^{m \rightarrow n}$ represents the coordinate transformation matrix from the parent to the new crystal. The basis $\mathbf{B}_{(ABC)'}^n$ expressed in the basis \mathbf{B}_{hex}^m is $\mathbf{B}_{(ABC)'}^m = \mathbf{T}_{hex}^{m \rightarrow n} \mathbf{B}_{(ABC)'}^n$. Therefore:

$$\mathbf{F}_{hex} \mathbf{B}_{ABC}^m = \mathbf{T}_{hex}^{m \rightarrow n} \mathbf{B}_{(ABC)'}^n \quad (\text{B.9})$$

or, equivalently:

$$\mathbf{F}_{hex} (\mathbf{C}_{hex}^{n \rightarrow m})^{-1} = \mathbf{T}_{hex}^{m \rightarrow n} \quad (\text{B.10})$$

where

$$\mathbf{C}_{hex}^{n \rightarrow m} = \mathbf{B}_{(ABC)'}^n (\mathbf{B}_{ABC}^m)^{-1} \quad (\text{B.11})$$

For further information about the general formulæ refer to Ref. [23].

The calculation leads to:

$$\mathbf{C}_{hex}^{n \rightarrow m} = \begin{pmatrix} -1 & 0 & 0 \\ 0 & -2/3 & -5/3 \\ 0 & -1/3 & 2/3 \end{pmatrix} \quad (\text{B.12})$$

$$\mathbf{T}_{hex}^{n \rightarrow m} = \begin{pmatrix} -1 & 0.1351 & -0.6407 \\ 0 & -0.7296 & -1.2814 \\ 0 & -0.3648 & 0.7296 \end{pmatrix} \quad (\text{B.13})$$

We remind that matrices equivalent to $\mathbf{T}_{hex}^{n \rightarrow m}$ and $\mathbf{C}_{hex}^{n \rightarrow m}$ can be obtained by multiplying $\mathbf{T}_{hex}^{n \rightarrow m}$ and $\mathbf{C}_{hex}^{n \rightarrow m}$ by the matrices of internal symmetry \mathbf{M}_{hex} of the hexagonal phase (matrices forming the point group of the hcp phase [61]). In other words:

$$\mathbf{C}_{hex}^{n \rightarrow m} = \mathbf{M}_{hex} \mathbf{C}_{hex}^{n \rightarrow m} = \begin{pmatrix} -1 & 0 & 0 \\ 0 & -1 & 0 \\ 0 & 0 & 1 \end{pmatrix} \begin{pmatrix} -1 & 0 & 0 \\ 0 & -2/3 & -5/3 \\ 0 & -1/3 & 2/3 \end{pmatrix} = \begin{pmatrix} 1 & 0 & 0 \\ 0 & 2/3 & 5/3 \\ 0 & -1/3 & 2/3 \end{pmatrix} \quad (\text{B.14})$$

$$\begin{aligned} \mathbf{T}_{hex}^{n \rightarrow m} = \mathbf{M}_{hex} \mathbf{T}_{hex}^{n \rightarrow m} &= \begin{pmatrix} -1 & 0 & 0 \\ 0 & -1 & 0 \\ 0 & 0 & 1 \end{pmatrix} \begin{pmatrix} -1 & 0.1351 & -0.6407 \\ 0 & -0.7296 & -1.2814 \\ 0 & -0.3648 & 0.7296 \end{pmatrix} \\ &= \begin{pmatrix} 1 & -0.1351 & 0.6407 \\ 0 & 0.7296 & 1.2814 \\ 0 & -0.3648 & 0.7296 \end{pmatrix} \end{aligned} \quad (\text{B.15})$$

which correspond to those of Eq. (3) and Eq. (4) in the main text.

Through Eq. (A.2), one can observed that the following conversions are fulfilled:

$$\begin{aligned} (0\bar{1}12)_m &\rightarrow (0003)_n \\ (0003)_m &\rightarrow (0\bar{1}12)_n \\ (0\bar{1}15)_m &\rightarrow (0\bar{1}15)_n \end{aligned} \quad (\text{B.16})$$

which correspond to what graphically evincible from Figure B-1.

References:

- [1] M.H. Yoo, J.K. Lee, Deformation twinning in h.c.p. metals and alloys, *Philos. Mag. A Phys. Condens. Matter, Struct. Defects Mech. Prop.* 63 (1991) 987–1000. <https://doi.org/10.1080/01418619108213931>.
- [2] J.W. Christian, S. Mahajan, Deformation twinning, *Prog. Mater. Sci.* 39 (1995) 1–157. [https://doi.org/10.1016/0079-6425\(94\)00007-7](https://doi.org/10.1016/0079-6425(94)00007-7).
- [3] J. Koike, Enhanced deformation mechanisms by anisotropic plasticity in polycrystalline Mg alloys at room temperature, in: *Metall. Mater. Trans. A Phys. Metall. Mater. Sci.*, 2005: pp. 1689–1696. <https://doi.org/10.1007/s11661-005-0032-4>.
- [4] C.M. Byer, B. Li, B. Cao, K.T. Ramesh, Microcompression of single-crystal magnesium, *Scr. Mater.* 62 (2010) 536–539. <https://doi.org/10.1016/j.scriptamat.2009.12.017>.
- [5] B. Syed, J. Geng, R.K. Mishra, K.S. Kumar, [0 0 0 1] Compression response at room temperature of single-crystal magnesium, *Scr. Mater.* 67 (2012) 700–703. <https://doi.org/10.1016/j.scriptamat.2012.06.036>.
- [6] E. Lilleodden, Microcompression study of Mg (0 0 0 1) single crystal, *Scr. Mater.* 62 (2010) 532–535. <https://doi.org/10.1016/j.scriptamat.2009.12.048>.
- [7] W.D. Russell, N.R. Bratton, Y.R. Paudel, R.D. Moser, Z.B. McClelland, C.D. Barrett, A.L. Oppedal, W.R. Whittington, H. Rhee, S. Mujahid, B. Paliwal, S.C. Vogel, H. El Kadiri, In situ characterization of the effect of twin-microstructure interactions on {1012} tension and {1011} contraction twin nucleation, growth and damage in magnesium, *Metals (Basel)*. 10 (2020) 1–23. <https://doi.org/10.3390/met10111403>.
- [8] M.R. Barnett, Twinning and the ductility of magnesium alloys. Part II. “Contraction” twins, *Mater. Sci. Eng. A*. 464 (2007) 8–16. <https://doi.org/10.1016/j.msea.2007.02.109>.
- [9] J. Peng, Z. Zhang, P. Guo, J. Huang, Y. Li, W. Zhou, Y. Wu, The effect of contraction twins and shear bands on the texture evolution during isothermal annealing and its effect on mechanical properties of AZ31 magnesium alloys, *Mater. Sci. Eng. A*. 763 (2019). <https://doi.org/10.1016/j.msea.2019.138100>.
- [10] P. Cizek, M.R. Barnett, Characteristics of the contraction twins formed close to the fracture surface in Mg-3Al-1Zn alloy deformed in tension, *Scr. Mater.* 59 (2008) 959–962. <https://doi.org/10.1016/j.scriptamat.2008.06.041>.
- [11] Q. Yu, L. Qi, K. Chen, R.K. Mishra, J. Li, A.M. Minor, The nanostructured origin of deformation twinning, *Nano Lett.* 12 (2012) 887–892. <https://doi.org/10.1021/nl203937t>.
- [12] M.A. Meyers, O. Vöhringer, V.A. Lubarda, The onset of twinning in metals: A constitutive description, *Acta Mater.* 49 (2001) 4025–4039. [https://doi.org/10.1016/S1359-6454\(01\)00300-7](https://doi.org/10.1016/S1359-6454(01)00300-7).
- [13] A. Chapuis, J.H. Driver, Temperature dependency of slip and twinning in plane strain compressed magnesium single crystals, *Acta Mater.* 59 (2011) 1986–1994. <https://doi.org/10.1016/j.actamat.2010.11.064>.
- [14] Y. Liu, P. Mao, F. Zhang, Z. Liu, Z. Wang, Effect of temperature on the anisotropy of AZ31 magnesium alloy rolling sheet under high strain rate deformation, *Philos. Mag.* 98 (2018) 1068–1086. <https://doi.org/10.1080/14786435.2018.1427896>.

- [15] H. Wang, P. Wu, S. Kurukuri, M.J. Worswick, Y. Peng, D. Tang, D. Li, Strain rate sensitivities of deformation mechanisms in magnesium alloys, *Int. J. Plast.* 107 (2018) 207–222. <https://doi.org/10.1016/j.ijplas.2018.04.005>.
- [16] M.R. Barnett, A Taylor model based description of the proof stress of magnesium AZ31 during hot working, *Metall. Mater. Trans. A Phys. Metall. Mater. Sci.* 34 A (2003) 1799–1806. <https://doi.org/10.1007/s11661-003-0146-5>.
- [17] B.Y. Liu, Z. Zhang, F. Liu, N. Yang, B. Li, P. Chen, Y. Wang, J.H. Peng, J. Li, E. Ma, Z.W. Shan, Rejuvenation of plasticity via deformation graining in magnesium, *Nat. Commun.* 13 (2022). <https://doi.org/10.1038/s41467-022-28688-9>.
- [18] The theory of the crystallography of deformation twinning, *Proc. R. Soc. London. Ser. A. Math. Phys. Sci.* 288 (1965) 240–255. <https://doi.org/10.1098/rspa.1965.0216>.
- [19] A. Ostapovets, A. Serra, Review of non-classical features of deformation twinning in HCP metals and their description by disconnection mechanisms, *Metals (Basel)*. 10 (2020) 1–20. <https://doi.org/10.3390/met10091134>.
- [20] C. Cayron, R. Logé, Evidence of new twinning modes in magnesium questioning the shear paradigm, *J. Appl. Crystallogr.* 51 (2018) 809–817. <https://doi.org/10.1107/S1600576718005678>.
- [21] C. Cayron, Hard-sphere displacive model of deformation twinning in hexagonal close-packed metals. Revisiting the case of the (56° , a) contraction twins in magnesium, *Acta Crystallogr. Sect. A Found. Adv.* 73 (2017) 346–356. <https://doi.org/10.1107/S2053273317005459>.
- [22] C. Cayron, The concept of axial weak twins, *Acta Mater.* (2022). <https://dx.doi.org/10.2139/ssrn.4073482>.
- [23] C. Cayron, Hard-sphere displacive model of extension twinning in magnesium, *Mater. Des.* 119 (2017) 361–375. <https://doi.org/10.1016/j.matdes.2017.01.047>.
- [24] G. Guillonneau, M. Mieszala, J. Wehrs, J. Schwiedrzik, S. Grop, D. Frey, L. Philippe, J.M. Breguet, J. Michler, J.M. Wheeler, Nanomechanical testing at high strain rates: New instrumentation for nanoindentation and microcompression, *Mater. Des.* 148 (2018) 39–48. <https://doi.org/10.1016/j.matdes.2018.03.050>.
- [25] D. Casari, L. Pethö, P. Schürch, X. Maeder, L. Philippe, J. Michler, P. Zysset, J. Schwiedrzik, A self-aligning microtensile setup: Application to single-crystal GaAs microscale tension-compression asymmetry, *J. Mater. Res.* 34 (2019) 2517–2534. <https://doi.org/10.1557/jmr.2019.183>.
- [26] S. Kalácska, J. Ast, P.D. Ispánovity, J. Michler, X. Maeder, 3D HR-EBSD Characterization of the plastic zone around crack tips in tungsten single crystals at the micron scale, *Acta Mater.* 200 (2020) 211–222. <https://doi.org/10.1016/j.actamat.2020.09.009>.
- [27] E.W. Kelley, J.W.F. Hosford, Plane strain compression of magnesium and magnesium alloy crystals, *Metall. Soc. Am. Inst. Mining, Metall. Pet. Eng. -- Trans.* 242 (1968) 5–13.
- [28] H. Conrad, W.D. Robertson, Effect of temperature on the flow stress and strain-hardening coefficient of magnesium single crystals, *Jom.* 9 (1957) 503–512. <https://doi.org/10.1007/bf03397908>.
- [29] O. Bauer, O. Vollenbruck, G. Schikorr, E. Schmid, W. Boas, P. Beck, M. Polanyi, G. Wassermann, W. Fahrenhorst, G. Siebel, W. Stenzel, J. Weerts, K. Weißenberger, E. Goens, G. Sachs, E. Schmid, *Beiträge*

- zur Physik und Metallographie des Magnesiums, in: *Mitteilungen Der Dtsch. Mater.*, 1932: pp. 16–25. https://doi.org/10.1007/978-3-642-92044-8_2.
- [30] R.E. Reed-Hill, W.D. Robertson, Deformation of magnesium single crystals by nonbasal slip, *Jom.* 9 (1957) 496–502. <https://doi.org/10.1007/bf03397907>.
- [31] A. Couret, D. Caillard, An in situ study of prismatic glide in HCP metals, *Rev. Phys. Appliquée.* 23 (1988) 667–667. <https://doi.org/10.1051/rphysap:01988002304066700>.
- [32] J. Jeong, M. Alfreider, R. Konetschnik, D. Kiener, S.H. Oh, In-situ TEM observation of $\{101\bar{2}\}$ twin-dominated deformation of Mg pillars: Twinning mechanism, size effects and rate dependency, *Acta Mater.* 158 (2018) 407–421. <https://doi.org/10.1016/j.actamat.2018.07.027>.
- [33] W.F. Hosford, E.W. Kelley, Plane-Strain Compression of Magnesium and Magnesium Alloy Crystals, *Trans. Metall. Soc. AIME.* 242 (1968) 5–13.
- [34] H. Tonda, K. Nakamura, K. Takashima, $\{112\bar{2}\} \langle 1123 \rangle$ Slip in Magnesium Single Crystal, *J. Japan Inst. Light Met.* 42 (1992) 765–771. <https://doi.org/10.2464/jilm.42.765>.
- [35] J. Ast, G. Mohanty, Y. Guo, J. Michler, X. Maeder, In situ micromechanical testing of tungsten micro-cantilevers using HR-EBSD for the assessment of deformation evolution, *Mater. Des.* 117 (2017) 265–266. <https://doi.org/10.1016/j.matdes.2016.12.052>.
- [36] Y. Guo, J. Schwiedrzik, J. Michler, X. Maeder, On the nucleation and growth of $\{112\bar{2}\}$ twin in commercial purity titanium: In situ investigation of the local stress field and dislocation density distribution, *Acta Mater.* 120 (2016) 292–301. <https://doi.org/10.1016/j.actamat.2016.08.073>.
- [37] J.R. Greer, J.T.M. De Hosson, Plasticity in small-sized metallic systems: Intrinsic versus extrinsic size effect, in: *Prog. Mater. Sci.*, 2011: pp. 654–724. <https://doi.org/10.1016/j.pmatsci.2011.01.005>.
- [38] M.D. Uchic, D.M. Dimiduk, J.N. Florando, W.D. Nix, Sample dimensions influence strength and crystal plasticity, *Science (80-.)*. 305 (2004) 986–989. <https://doi.org/10.1126/science.1098993>.
- [39] M.D. Uchic, P.A. Shade, D.M. Dimiduk, Plasticity of micrometer-scale single crystals in compression, *Annu. Rev. Mater. Res.* 39 (2009) 361–386. <https://doi.org/10.1146/annurev-matsci-082908-145422>.
- [40] N.M. Della Ventura, S. Kalácska, D. Casari, T.E.J. Edwards, A. Sharma, J. Michler, R. Logé, X. Maeder, $\{101\bar{2}\}$ twinning mechanism during in situ micro-tensile loading of pure Mg: Role of basal slip and twin-twin interactions, *Mater. Des.* 197 (2021). <https://doi.org/10.1016/j.matdes.2020.109206>.
- [41] N.M. della Ventura, A. Sharma, S. Kalácska, M. Jain, T.E.J. Edwards, C. Cayron, R. Logé, J. Michler, X. Maeder, Evolution of deformation twinning mechanisms in magnesium from low to high strain rates, *Mater. Des.* 217 (2022). <https://doi.org/10.1016/j.matdes.2022.110646>.
- [42] M.D. Nave, M.R. Barnett, Microstructures and textures of pure magnesium deformed in plane-strain compression, *Scr. Mater.* 51 (2004) 881–885. <https://doi.org/10.1016/j.scriptamat.2004.07.002>.
- [43] BEVIS M, CROCKER AG, Twinning Modes in Lattices, 313 (1969) 590–529.
- [44] M.R. Barnett, Z. Keshavarz, A.G. Beer, X. Ma, Non-Schmid behaviour during secondary twinning in a polycrystalline magnesium alloy, *Acta Mater.* 56 (2008) 5–15. <https://doi.org/10.1016/j.actamat.2007.08.034>.
- [45] H. Yoshinaga, T. Obara, S. Morozumi, Twinning deformation in magnesium compressed along the C-

- axis, *Mater. Sci. Eng.* 12 (1973) 255–264. [https://doi.org/10.1016/0025-5416\(73\)90036-0](https://doi.org/10.1016/0025-5416(73)90036-0).
- [46] L. Jiang, J.J. Jonas, A.A. Luo, A.K. Sachdev, S. Godet, Twinning-induced softening in polycrystalline AM30 Mg alloy at moderate temperatures, *Scr. Mater.* 54 (2006) 771–775. <https://doi.org/10.1016/j.scriptamat.2005.11.029>.
- [47] L. Jiang, M. Gong, J. Wang, Z. Pan, X. Wang, D. Zhang, Y.M. Wang, J. Ciston, A.M. Minor, M. Xu, X. Pan, T.J. Rupert, S. Mahajan, E.J. Lavernia, I.J. Beyerlein, J.M. Schoenung, Visualization and validation of twin nucleation and early-stage growth in magnesium, *Nat. Commun.* 13 (2022). <https://doi.org/10.1038/s41467-021-27591-z>.
- [48] B.Y. Liu, J. Wang, B. Li, L. Lu, X.Y. Zhang, Z.W. Shan, J. Li, C.L. Jia, J. Sun, E. Ma, Twinning-like lattice reorientation without a crystallographic twinning plane, *Nat. Commun.* 5 (2014). <https://doi.org/10.1038/ncomms4297>.
- [49] K.Y. Xie, K. Hazeli, N. Dixit, L. Ma, K.T. Ramesh, K.J. Hemker, Twin boundary migration mechanisms in quasi-statically compressed and plate-impacted mg single crystals, *Sci. Adv.* 7 (2021). <https://doi.org/10.1126/sciadv.abg3443>.
- [50] Y. He, B. Li, C. Wang, S.X. Mao, Direct observation of dual-step twinning nucleation in hexagonal close-packed crystals, *Nat. Commun.* 11 (2020). <https://doi.org/10.1038/s41467-020-16351-0>.
- [51] C. Cayron, Complements to mügge and friedel’s theory of twinning, *Metals (Basel)*. 10 (2020). <https://doi.org/10.3390/met10020231>.
- [52] Twinning shears in lattices, *Proc. R. Soc. London. Ser. A. Math. Phys. Sci.* 304 (1968) 123–134. <https://doi.org/10.1098/rspa.1968.0077>.
- [53] T.A. Parthasarathy, S.I. Rao, D.M. Dimiduk, M.D. Uchic, D.R. Trinkle, Contribution to size effect of yield strength from the stochastics of dislocation source lengths in finite samples, *Scr. Mater.* 56 (2007) 313–316. <https://doi.org/10.1016/j.scriptamat.2006.09.016>.
- [54] S.H. Oh, M. Legros, D. Kiener, G. Dehm, In situ observation of dislocation nucleation and escape in a submicrometre aluminium single crystal, *Nat. Mater.* 8 (2009) 95–100. <https://doi.org/10.1038/nmat2370>.
- [55] D. Hull, D.J. Bacon, *Introduction to Dislocations*, 2011. <https://doi.org/10.1016/C2009-0-64358-0>.
- [56] S. Ando, M. Tsushida, H. Kitahara, Deformation behavior of magnesium single crystal in c-axis compression and a-axis tension, in: *Mater. Sci. Forum*, 2010: pp. 699–702. <https://doi.org/10.4028/www.scientific.net/MSF.654-656.699>.
- [57] L. Wen, P. Chen, Z.F. Tong, B.Y. Tang, L.M. Peng, W.J. Ding, A systematic investigation of stacking faults in magnesium via first-principles calculation, *Eur. Phys. J. B.* 72 (2009) 397–403. <https://doi.org/10.1140/epjb/e2009-00365-2>.
- [58] C. Slater, N. Tamanna, C. Davis, Optimising compression testing for strain uniformity to facilitate microstructural assessment during recrystallisation, *Results Mater.* 11 (2021). <https://doi.org/10.1016/j.rinma.2021.100218>.
- [59] G.D. Sim, G. Kim, S. Lavenstein, M.H. Hamza, H. Fan, J.A. El-Awady, Anomalous hardening in magnesium driven by a size-dependent transition in deformation modes, *Acta Mater.* 144 (2018) 11–20. <https://doi.org/10.1016/j.actamat.2017.10.033>.

- [60] Z. Zhang, Twinning and its related work hardening during the ambient extrusion of a magnesium alloy, *Mater. Sci. Eng. A*. 577 (2013) 125–137. <https://doi.org/10.1016/j.msea.2013.03.078>.
- [61] C. Cayron, Groupoid of orientational variants, *Acta Crystallogr. Sect. A Found. Crystallogr.* 62 (2006) 21–40. <https://doi.org/10.1107/S010876730503686X>.